Stabilizing a diode laser onto the $^1S_0 \rightarrow {}^3P_1$ intercombination line of strontium

Towards an ultracold strontium experiment

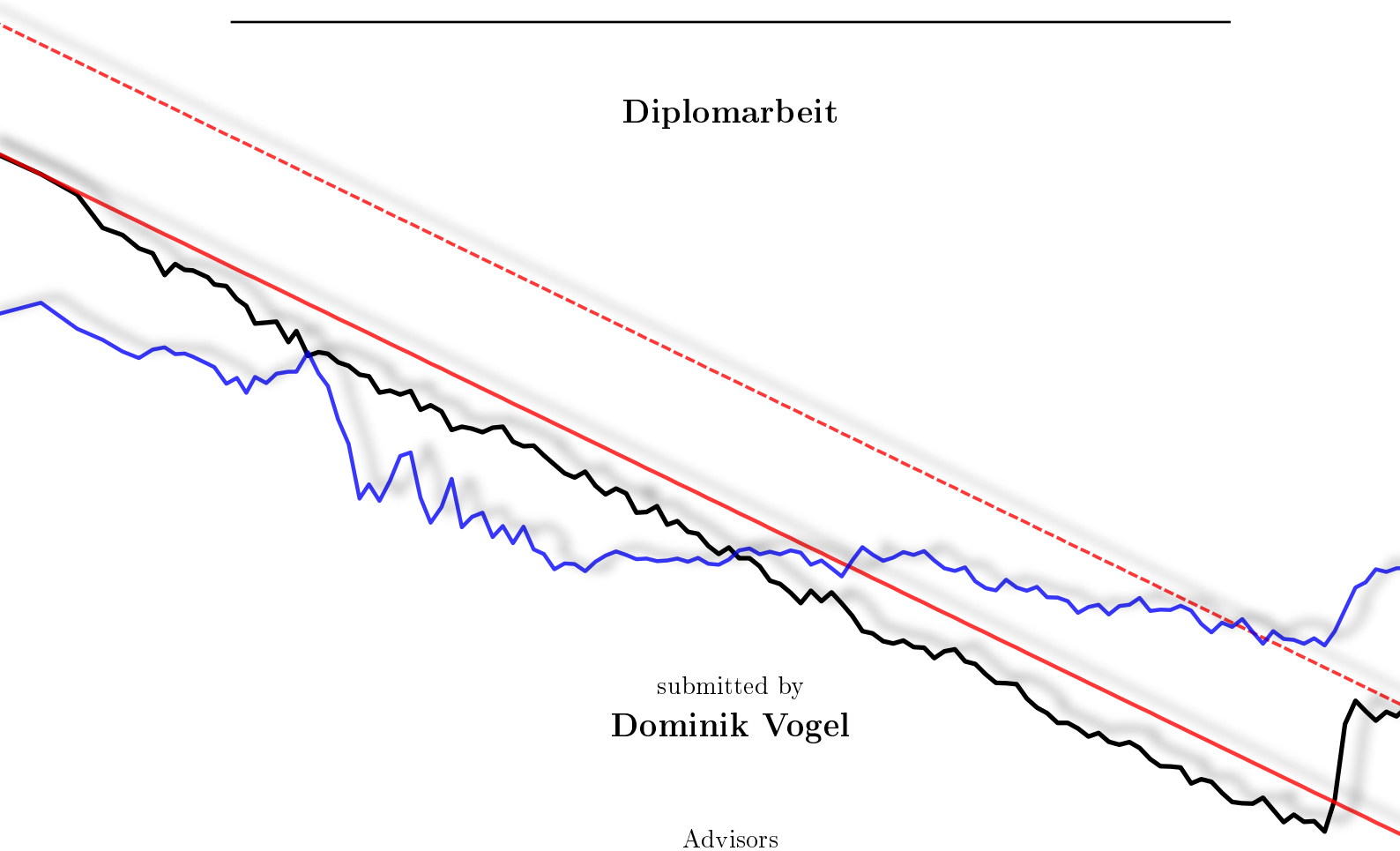

Diplomarbeit

submitted by

Dominik Vogel

Advisors

Prof. Dr. Claus Zimmermann

Arbeitsgruppe Quantenoptik

Physikalisches Institut III

Eberhard Karls Universität Tübingen

Prof. Dr. Philippe W. Courteille

Grupo de Ôptica Atômica

Departamento de Física e Ciência dos Materiais

Instituto de Física em São Carlos

Universidade de São Paulo

January 2012

Contents

1 Introduction

Since the very beginning of science there have been curious people driven by their fundamental urge to understand the intriguing world that surrounds us all a little bit better. With steady technological advances new tools became available and allowed us to find answers to questions about unsolved riddles.

For example, in 1960 Theodore Maimann [25] accomplished the first step in the development of the laser, which became an extremely versatile tool for the manipulation and investigation of matter properties during the following decades, even though at the time of its invention applications seemed to be lacking. One of the areas in which the laser became a crucial element is the field of cold atoms. In 1953 Wolfgang Paul [28] built an experiment to trap single ions, which were easier to handle than atoms, because of their electric charge. For electrically neutral atoms only the coherent light field of a laser interacting with their internal oscillating charges made it possible to gain sufficient control to slow and trap clouds of atoms. Prichard et al. were the first to realize a so called magneto optical trap (MOT) [29], in which they trapped ten million sodium atoms and cooled them down to a temperature of 0.4K above absolute zero. The importance of cooling atoms can be made clear by the following comparison: imagine you should find out in detail how cars work, but instead of opening the hub in a garage you may only observe them from the side of an highway. Similarly atoms in a thermal gas move at speeds of several hundred kilometers per hour and slow down to, when cooled in a MOT, a movement of a few millimeters per second. Another reason for the interest in cooling atoms was the prediction of a novel state of matter, which has already been predicted in 1924 by Albert Einstein and Satyendranath Bose [13] . 71 years later this new state of matter called Bose Einstein condensate (BEC) has been achieved by the group of E.A. Cornell by cooling a cloud of rubidium atoms. This and the following BEC experiments offered new insights into the fundamental physical laws of quantum mechanics, because slowed atoms do not behave as classical mechanics would predict.

To further study the atomic interactions BECs of other species than rubidium were tried to be created. A calcium condensate [21] was the first of an atomic species that has more than one valence electron. Only half a year later in 2009 the first strontium, also an earth alkali, condensate was realized [35]. The electronic structure of strontium offers many new unexplored possibilities for cold atom experiments and was therefore chosen for the experiment that is described in the course of this work.

One principal difference of atoms with two valence electrons to atoms with only one is, that their electronic level structure includes finer transitions, called inter-combination lines. This means they may interact strongly with light of a certain

frequency but show no reaction towards light of a slightly different frequency. Again, the significance of the laser as a precise tool becomes lucid, as only with a laser of extremely well defined frequency this atomic transition can be driven. In the case of strontium such an intercombination line can be used for efficient cooling. Therefore a laser stabilized onto the resonance frequency of this line is essential for successfully conducting the experiment.

An excellent technique for stabilizing diode lasers via an electronic feedback loop and using a stable optical resonator as a frequency reference has been published by Pound, Drever and Hall [11] in 1983. This method has been employed [24] to stabilize a laser down to an emission bandwidth of less than one Hz.

This thesis describes the realization and evaluation of such a Pound Drever Hall (PDH) stabilization of a laser system which is going to be used for an experiment with ultracold strontium.

The **second chapter** gives a short overview over the current state of the strontium experiment and some strontium properties. The **third chapter** introduces the necessary concepts for understanding a PDH stabilization and presents the actual experimental setup. In the **fourth chapter** the results of the stabilization are discussed.

In order to interact with the strontium atom the used laser does not only need to be stabilized, it also requires the right frequency. In the **fifth chapter** a spectroscopy setup is described, which allows us to determine the current frequency of the laser relative to the atomic resonance. The resulting spectra are discussed in the **sixth chapter**.

The last chapter consists of a summary of this work and provides an outlook on the next steps.

2 Strontium experiment

This chapter describes briefly the ultracold strontium experiment that has been launched in December 2010 in a new lab at the Instituto de Física in São Carlos by Prof. Dr. W. Courteille. In the first section the general properties of strontium are presented, in the second the cooling cycle is summed up and in the third section the current state of the experimental apparatus is described.

2.1 Relevant properties of strontium

2.1.1 Electronic structure

Strontium is an alkaline earth metal with 38 electrons and is Helium-like, i.e. it has two valence electrons that significantly interact with each other.

2.1.1.1 Ground state

The electronic structure including all electrons is shown in fig. 2.1. The low energy excitations, i.e. in the optical regime, affecting only the two valence electrons, will be discussed in detail later (see fig. 2.2), but are already shown above the horizontal dotted line to give an overview.

The ground state is denominated by

$$\left[1s^2 2s^2 2p^6 3s^2 3p^6 4s^2 3d^{10} 4p^6\right]\ 5^1S_0$$

It is notable that due to the electron-electron interaction energy there is no more degeneracy of the l quantum number so that states with a smaller orbital angular momentum are favored, since their spacial probability distribution is centered closer to the nucleus, this means that they therefore experience less of the shielding effect caused by the other electrons. This effect becomes that strong, that the 4s-state is populated before completing the third shell and also the 5^1S_0-state becomes the ground state even though the fourth shell is not completed.

2.1.1.2 Excitations

The electronic structure for the most relevant optically excited states of the two valence electrons is shown in fig. 2.2.

The scheme only shows the excitations of one of the two electrons in the fifth shell ($(5s^2)^1S_0$), while the other remains on the 5s-level. All other excitations,

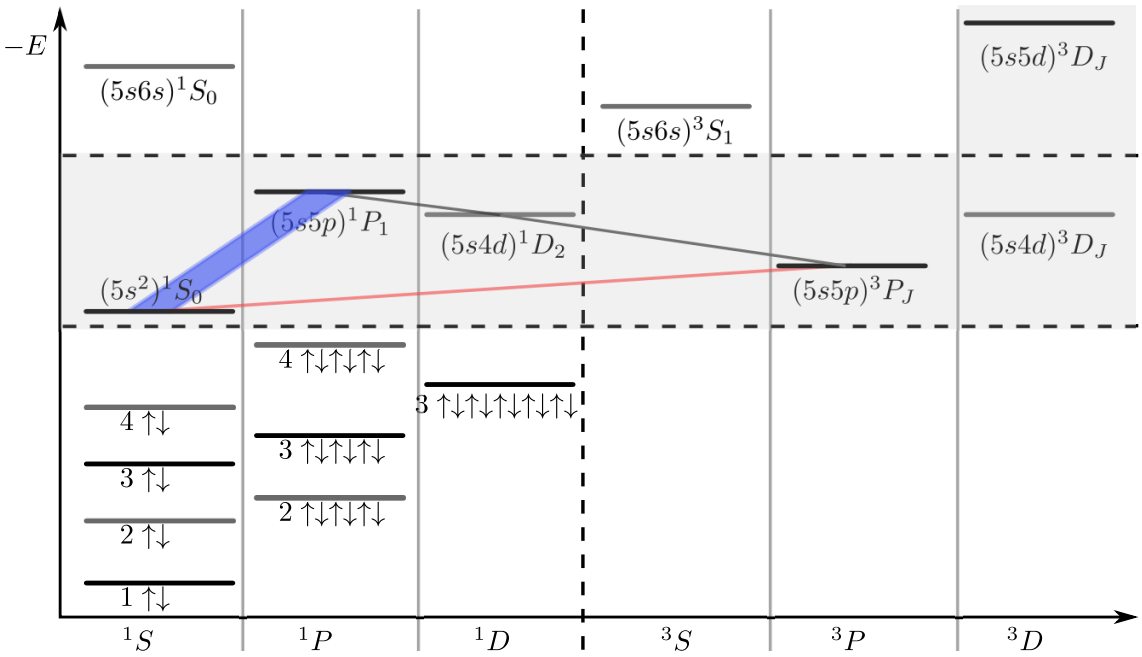

Figure 2.1: Electronic level scheme of bosonic Stronitum. The filled states with lower energies than $(5s^2)^1S_0$ have been omitted.

including two electrons or lower electrons are of higher energy and are not relevant for this experiment.

As the two involved electrons are indistinguishable and the Hamiltonian only depends on the total spin S, the energy-eigenstates shown in fig. 2.2 are two electron states which can be described by a linear superposition of the single electron states, similar to the Helium atom.

The scheme is divided into two sides by a vertical dotted line. The left side depicts all singlet-states ($S = 0$), while the right side shows triplets of states due to the three different orientations of the spin ($S = 1$) relative to the total orbital angular momentum.

Besides the separation in singlet and triplet systems there is no further analogy to Helium for those states, as most of them do not exist in helium. In contrast to helium there is the $(5s4p)^1D_2$-state from the incomplete fourth shell which cannot be excited directly from the ground state because of the dipole selection rule $\Delta J = 0, \pm 1$. The $(5s5p)^1P_1$-state appears as we are already populating the fifth shell, where there is no degeneracy of orbital angular momentum. The transition from the ground state is strongly coupled with a linewidth of 32MHz to a light field with a wavelength of 460.73nm.

The corresponding triplet $(5s5p)^3P_J$ with one spin flipped, and thus antisymmetric spacial wavefunction and with less electron repulsion, forms the metastable ground state of the triplet system.

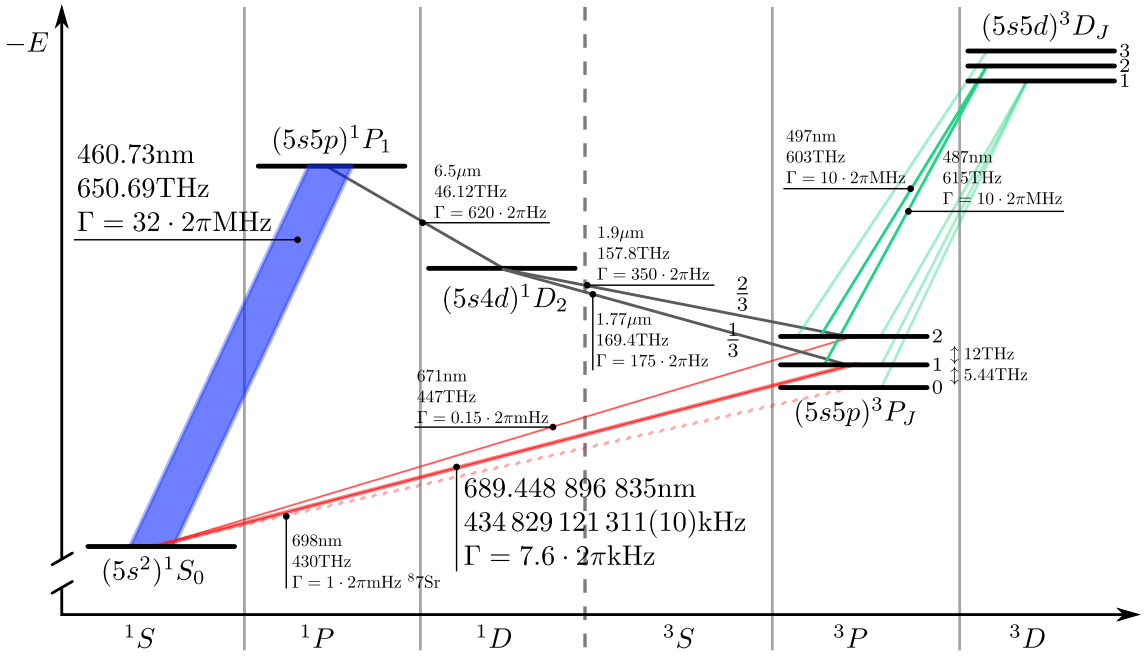

Figure 2.2: Electronic level scheme of ^{88}Sr. The filled states with lower energies than $(5s^2)^1S_0$ have been omitted.

isotope	abundance	mass [in u]	nuclear spin	scattering length
^{88}Sr	82.58%	87.906	0	$-2a_0$[27]
^{87}Sr	7.00%	86.909	$\frac{9}{2}$	
^{86}Sr	9.86%	85.909	0	$+800a_0$[34]
^{84}Sr	0.56%	83.913	0	$+123a_0$[35]

Table 2.1: Natural abundance, mass, nuclear spin [32] and scattering length of the four stable strontium isotopes.

2.1.2 Isotopes

There are four stable Sr isotopes, of which three are bosonic (^{88}Sr, ^{86}Sr, ^{84}Sr) and one fermionic (^{87}Sr). Their natural abundance, mass, nuclear spin [32] and scattering length, are summed up in table 2.1.

2.1.3 Strontium vapor

The melting point of strontium is at 769°C the boiling point at 1384°C[4].

For the vapor pressure there are different values in the literature. Fig. 2.3 sums those up.

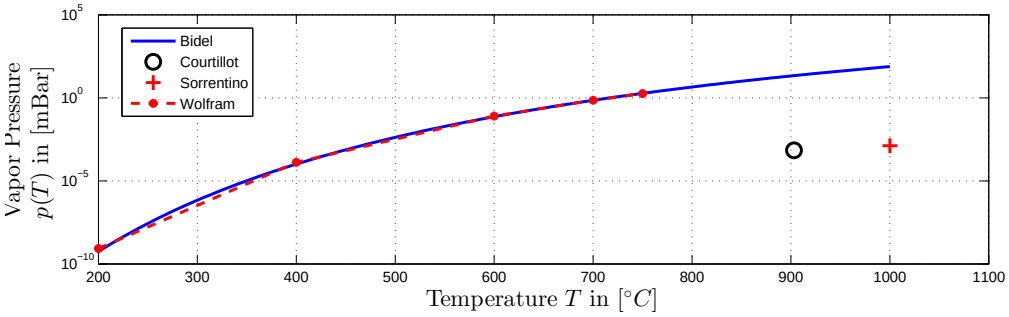

Figure 2.3: Semi-logrithmical graph of the vapor pressure of strontium as a function of temperature comparing different information sources: Bidel [4] refers to [17], while Sorrentino[32] does not give any reference. Courtilliot[8] mentions the disagreement of two orders of magnitude of their measurements and the ones from Dinneen[37] with others like [22] which is mentioned as a source by Wolfram[2].

The atomic density can be derived by applying the equation of state of a classical ideal gas

$$n(T) = \frac{p(T)}{k_B T} \tag{2.1}$$

The thermal Maxwell-Boltzmann distribution of an ideal gas is given by

$$P(v) = \sqrt{\frac{2}{\pi}\left(\frac{m}{kT}\right)^3}\, v^2 \mathrm{e}^{\left(\frac{-mv^2}{2kT}\right)}$$

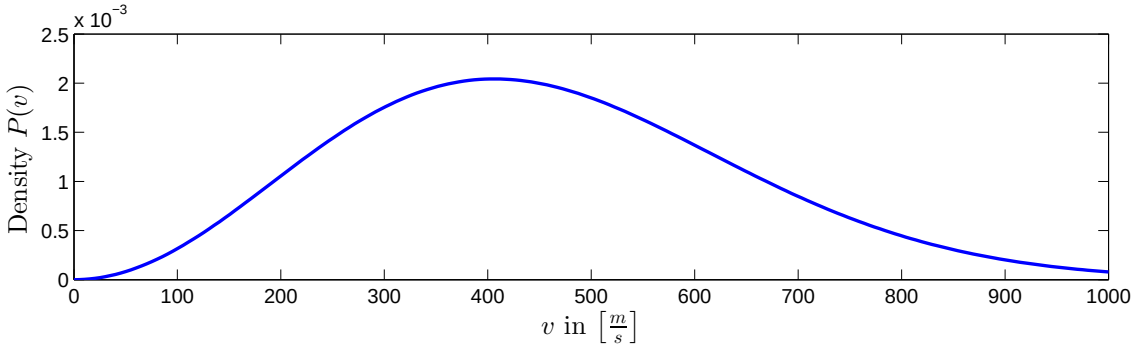

Figure 2.4: The probability density $P(v)$ plotted against the atomic velocity v of ^{88}Sr at 600°C.

as illustrated in fig. 2.4.The median $\hat{v}$ and mean $\bar{v}$ of this distribution is calculated as

$$\hat{v} = \sqrt{\frac{2k_\mathrm{B}T}{m}} \qquad \bar{v} = \sqrt{\frac{8kT}{\pi m}}$$

which gives $\hat{v} = 406\frac{\mathrm{m}}{\mathrm{s}}$at a temperature of 600°C.

2.1.4 Source & handling

Strontium is relatively easy and cheap to purchase. For the import it has to be taken into account that it is considered a dangerous good, because of its chemical reactivity. It oxidizes relative quickly, when exposed to air. For this reason it has to be handled under a protection atmosphere. For long time storage it can be submerged in mineral oil. When oxidized it turns from a silver color to pale yellow and becomes a powder. Strontium has a Mohs hardness of 1.5, which is similar to tin or lead[2]. Therefore motorized tools are very helpful for cutting.

Dispensers are not available to our knowledge. The cost for isotope purified strontium is tremendously high.

2.2 Cooling cycle

Strontium has a very advantageous electronic structure for laser cooling. It offers a 32MHz broad transition that is almost closed and a closed fine 7.6kHz transition, which is fine enough to cool down to the recoil limit, but strong enough to sustain the atoms against gravity. There are different ways how to take advantage of the variety of transitions. The cooling cycle aimed for in this experiment has already been employed [35] to cool strontium down to degeneracy. It can be divided in six steps

1. Producing strontium vapor in an oven at around 600°C

2. Slowing the thermal atomic beam from the oven using a Zeeman slower at the 32MHz ${}^1S_0 \rightarrow {}^1P_1$transition

3. Loading the first stage magneto optical trap (MOT) using the same transition. There is only a small loss channel via the ${}^1D_2$ level that eventually decays into the triplet ${}^3P_2$. Even though these states are not cooled further at this point they are trapped within the magnetic field gradient due to their magnetic moment. This means that while operating this first stage MOT the meta stable ${}^3P_2$ accumulates a population of cooled atoms.

4. Repumping: A laser beam at 497nm excites atoms in the ${}^3P_2$ to the ${}^3D_2$ state, from where they decay into the ${}^3P_1$ state and back into the ${}^3P_2$. Within a short time the population from the ${}^3P_2$ state is completely transferred to the ${}^3P_1$state.

5. The second stage MOT using the 7.6kHz${}^1S_0 \rightarrow {}^3P_1$ transition can be loaded from the cooled atoms in the ${}^3P_1$ state.

6. Evaporation out of an all optical dipole trap

2.3 Apparatus

In order to realize the cooling scheme that has been presented in the previous section, we are building a specialized experimental apparatus. Fig. 2.5 shows a picture of the still incomplete apparatus at the time of completion of this thesis. Underneath the picture a functional scheme has been added for better orientation.

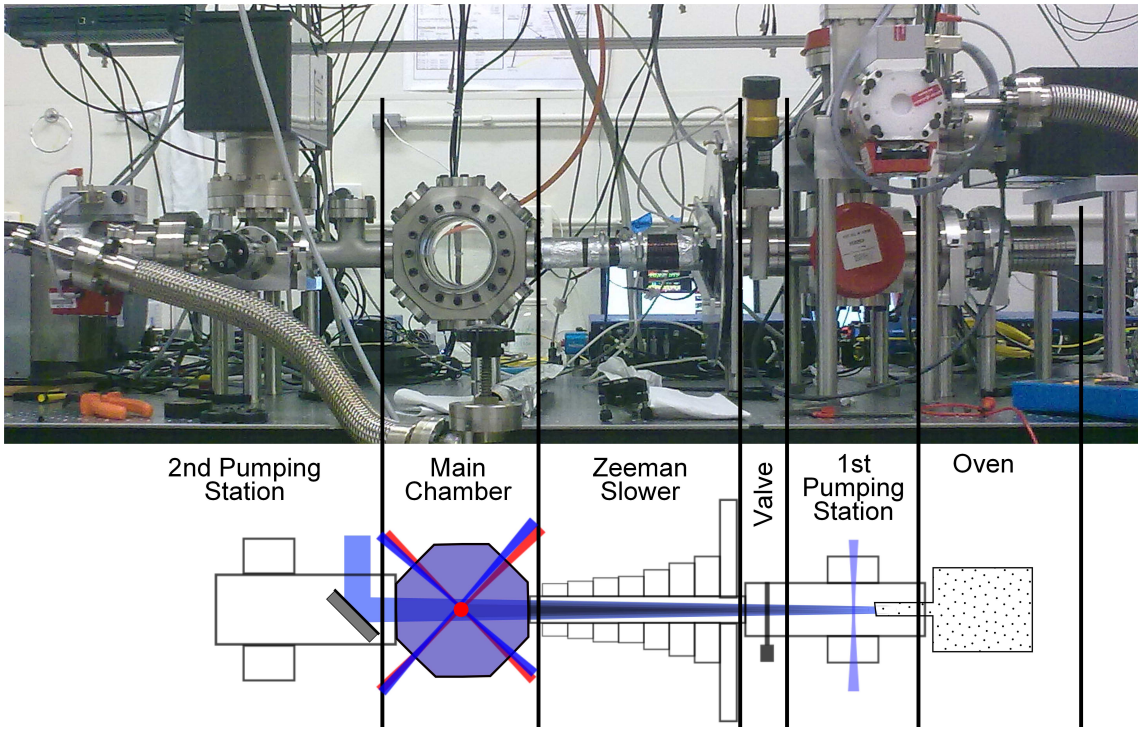

Figure 2.5: Photo and scheme of the strontium apparatus, without optics and MOT-coils.

Within this scheme the atoms travel within the cooling cycle from right to left. A thermal atomic beam is created within the oven by heating a reservoir of strontium up to temperatures around 600°C with a resistive heating wire. The part of the oven that is heated consists of a wide metal cylinder that reduces to a thin cylinder reaching into the adjacent six-way-cross in the next section. A guiding and thermal contact improving lane for the thermo-wire has been cut into the cylinder. The spiral path it follows has the highest winding density at the thin end, where the highest temperature is needed in order to avoid cloaking of the capillary nozzle that is screwed into the cylinder cap. The capillaries are formed by steel microtubes that are 1.2mm long and 330µm in diameter, which were obtained from standard medical injection needles cut with a high power laser. They are packed together to a round array of 9 mm diameter. For fine tuning the direction of the atomic beam emitted through the capillary tubes, the so far described construction is connected to the apparatus via a short bellow, that reaches into the six way cross and thus minimizes the radius to which the beam diverged at the central point of the main chamber.

In order to further reduce the divergence of the atomic beam, the six way cross in the next section offers four CF63 viewports through which an optical molasses on the principal blue 461nm can be formed. In the molasse the transverse movement of the atoms is cooled using standard Doppler cooling techniques. A detailed description on transverse cooling of strontium can be found in the PhD thesis of Y.Bidel [4]. On the top side the first pumping stage is attached, which consists of a 40l/sec ion pump and a turbo pump.

After passing a gate valve, the atoms enter into the Zeeman slower tube, which with an initial diameter of 9mm also acts as a differential pumping tube between the first and second pumping stations. The magnetic field is created by a flat 1x5mm copper wire. The number of windings is chosen in such a way, that in superposition with the field from the MOT coils that are going to be attached laterally to the main chamber, a field strength results which compensates the Doppler shift of the decelerated atoms at any point with the according Zeeman shift. Even though the number of windings is decreasing from right to left, the overall field is that of a so called spin flip Zeeman slower. That means that the Zeeman shift changes its sign with the inversion of the field direction, which in our case occurs in the last third of the slower. This has the advantage over increasing field geometries that faster atoms can be slowed with a lower maximum field and over decreasing field geometries is shows the advantage that the slowing beam is detuned from the transitions of the atoms trapped in the MOT.

The slowed atoms that leave the Zeeman slower enter into the main chamber. It was manufactured at the local mechanical workshop from a solid block of 316L steel. The octagonal shape with eight CF40 connections and two CF100 flanges was designed to offer optimal optical access and minimum volume.

To reach ultrahigh vacuum conditions, there is a second pumping station connected via a T to the main chamber. The T inhabits an additional 45° inclined mirror, which will guide the laser beam for Zeeman slowing from the side window onto the main axis. The reason for deviating the laser beam is that a window on the main axis would quickly become opaque due to the strontium beam that would coat it. Usually [32] a sapphire window, that is heated up to 450K is used. Using a mirror instead bears the advantage that no transparency but reflectivity is required, which might not be affected tremendously.

3 Frequency stabilization of the 689nm laser system

Any laser field created by a diode laser is subject to noise.That means that the created electromagnetic field cannot be described by a perfect sine wave with a specific frequency. These deviations are caused by uncontrolled changes of parameters that influence the lasing process. For example, noise of the driving current of the laser diode changes of length of the involved resonators due to vibrations, thermal noise and drifts, as well as electrical noise in case of the piezo crystal that determines the length of the resonator that is formed by the grating and the laser diode itself. For extremely stable systems even changes to the refraction index of the air the laser beam passes through, which are caused by temperature and pressure changes, may have an important impact.

For many research and high tech applications, a controlled and stable laser field is crucial. In the field of atom-optics, lasers are the principal tool for manipulating atoms. In our case, to achieve a Sr-BEC, we need a stable laser for efficiently operating a secondary MOT.

In order to attain a more stable field, there are two possibilities. Firstly, the fluctuations of the parameters of the lasing process can be reduced to a minimum and secondly, one can try to compensate for those uncontrolled fluctuations via a feedback loop. Extremely good results have been achieved by using the *Pound Drever Hall (PDH) Technique,* which has been developed in the early 1980s and has evolved to a standard in laser frequency stabilization.

To compare different systems and formulate prerequisites the term *stability* has to be quantified. In a more abstract context the laser field can be considered as a precision oscillator, for which extensive models have been developed in the mid-1960s [33] that define standards in measures of stability.

This chapter consists of three sections. In sec. 3.1 the PDH technique, which we used to stabilize the 689nm laser, is explained, in the following sec. 3.2 the theory necessary in order to quantify the achieved stability is introduced. And finally in sec. 3.3 the realization of the actual system is described.

3.1 The Pound Drever Hall technique

3.1.1 Electronic feedback loop

An electronic feedback loop is a signal loop between the system to be stabilized and an electronic controller device. From the system to the controller, an *error signal*

representing the deviation of the system from its desired state is transmitted. The loop is closed by the feedback signal transmitted from the controller to the system in order to steer it in such a way that the error signal is minimized.

In the case of the laser frequency stabilization loop, the error signal describes the frequency deviation of the laser field, and the feedback signal is directly fed into the laser diode, modulating the current and thus regulating the frequency.

3.1.2 Central idea

The central idea of the PDH technique concerns the *frequency discrimination*, that means determination of the current laser frequency. This is a difficult issue, because no electronics have been developed yet operating at the frequency of optical light, i.e. hundreds of THz, in order to measure the frequency directly. Even if there was such a quick circuit available, there still is the need of a reference oscillator that has a stability equal to or higher than the one aspired for the laser.

There are various techniques that solve this problem by using an optical setup[1]. As a reference a high finesse optical resonator, which is available with extremely high stability, is employed. The determination of the frequency deviation can be accomplished by using the frequency dependent reflection coefficient of an optical resonator defined as

$$F(\nu) = \frac{E_{refl}}{E_{in}}$$

where E_{refl} and E_{in} are the reflected and incident field amplitudes respectively. It describes the amplitude and phase of a the reflected beam. In the vicinity of a resonance frequency, it can be depicted as in fig. 3.1.

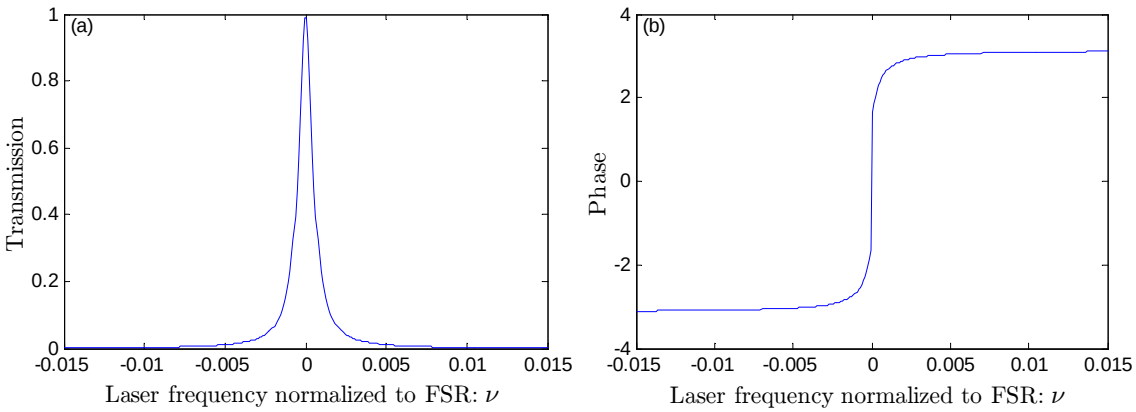

Figure 3.1: Amplitude(a) and phase(b) of the reflection coefficient $F(\nu)$ of an optical resonator with a finesse of 6000 and a free spectral range of 1.5GHz.

[1] A frequency comb is another approach to determine optical frequencies of a light field with high precision.

The most obvious solution, called *side of fringe locking*, consists of separating the reflected beam from the incoming with a combination of a polarizing beam splitter (PBS) and a $\frac{\lambda}{4}$-plate, and measure its intensity with a photodiode. The resulting electronic signal constitutes in first order a linear mapping to the laser frequency ν around the half maximum points, and can the be fed as an error signal to the controller, which regulates the system in such a way that a constant intensity is obtained at the diode which ideally corresponds to a fixed frequency.

The problem with this solution is that not only the laser frequency but also the laser intensity is subject to noise, thus the control electronics cannot distinguish between a frequency variation and an intensity variation, i.e. there would be a non-constant error signal even though the laser was stable and it would be destabilized by the control.

The idea of the PDH stabilization sets in at this point: to isolate the frequency noise, the error signal is taken from the reflected beam at resonance where the intensity, as well as its derivative with respect to ν, go to zero in an ideal case.

This, on the other hand, creates a different problem: the signal is symmetric to the setpoint and therefore does not carry any instantaneous information about the direction in which the control should counteract.

While the amplitude of $F(\nu)$ is symmetric around resonance, the phase (cf. fig. 3.1 (b)) is antisymmetric and reveals the desired information about, to which side the laser is detuned.

As there is no device or method developed to measure the phase of an optical em. field directly, interference is used in order to determine the phase. Imagine superimposing the following fields:

$$E_1 \propto \sin\left(2\pi\nu t + \varphi\right)$$
$$E_2 \propto \sin\left(2\pi\left(\nu - \delta\nu\right)t\right)$$

Where$E_1$is the field oscillating with ν near the resonance, and E_2 a field oscillating with a frequency shifted by $\delta\nu$ off resonance and a phase difference in respect with E_1 of φ. The interference term of the superimposed field[2] is a superposition of the sum-frequency and the difference frequency, while both carry the phaseshift:

$$\left(E_1 + E_2\right)^2 = E_1^2 + E_2^2 + \underbrace{2E_1E_2}_{\text{interference term}}$$
$$2E_1E_2 = \sin\left[2\pi\left(2\nu - \Omega\right)t + \varphi\right] + \sin\left(2\pi\Omega t + \varphi\right)$$

The resulting intensity thus carries the information about the phaseshift, this time oscillating at a frequency $\delta\nu$ which is much smaller than ν. Thus the phaseshift can be extracted electronically and, as will be shown later, constitutes a steep, non-symmetrical error signal.

[2]neglecting any amplitudes in the following

Taking advantage of the phaseshifting characteristics of an optical resonator, one can determine the actual laser frequency deviation from resonance by extracting the phaseshift of the reflected beam via interference. As the phaseshift is independent of the intensity of the incoming beam, the frequency noise is decoupled from the intensity noise.

3.1.3 Optical resonators

By the term *optical cavity resonator* (short: cavity/resonator) I want to refer to a device that basically consists of two high reflective mirrors that are positioned opposed to each other with a shared surface normal, separated by a distance L.

In such a setup the amplitude of electromagnetic modes within the cavity shows a strong frequency dependency, because of which it is called resonator.

Kogelnik and Li give a great review on the theory of resonators in[20]. For our experiment it was important to decide on the parameters of the cavity, to perform a *mode match* i.e. to couple a laser beam in such a way to the resonator that the maximum amplitude is transferred to the desired mode and, to perform the stabilization, to understand the reflection off a Fabry–Pérot interferometer as a model for our cavity.

3.1.3.1 The Fabry–Pérot interferometer

A Fabry–Pérot interferometer consists of two parallel plane mirrors as shown in fig 3.2. An incident beam will be reflected between the mirrors, while for each reflection there is a leakage. So the initial beam will be partially reflected and partially transmitted. The complex overall reflection coefficient can be calculated summing up the partial beams with the correct optical path difference[3] $\delta = 2kL$, with the wavenumber k and mirror distance L, and amplitudes determined by the mirror

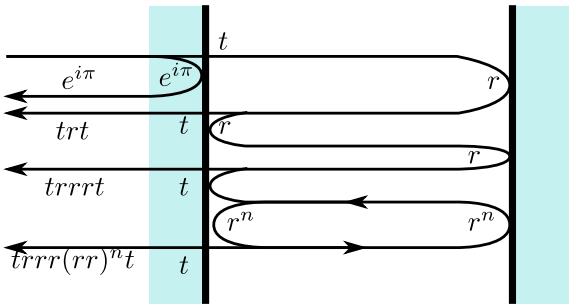

Figure 3.2: Stylized interference of the paths reflecting a beam off an FPI.

[3] There is a π-phase shift for the very first reflection.

reflection and transmission coefficients r ant t.

$$\begin{aligned} F(\nu) &= re^{i\pi} + t^2 re^{i\delta} \sum_{n=0}^{\infty} (rr)^n e^{in\delta} = -r + t^2 re^{i\delta} \sum_{n=0}^{\infty} \left(r^2 e^{i\delta}\right)^n \\ &= -r + \frac{re^{i\delta}t^2}{1 - r^2 e^{i\delta}} = \frac{-r + r^3 e^{i\delta} + re^{i\delta}(1 - r^2)}{1 - r^2 e^{i\delta}} \\ F(\nu) &= \frac{r\left(e^{i\delta} - 1\right)}{1 - r^2 e^{i\delta}} \end{aligned} \tag{3.1}$$

The frequency dependence of the reflection coefficient $F(\nu)$ is called *airy formula*[4].

The ν dependence is entirely included within

$$e^{i\delta} = e^{ik2L} = e^{i2\pi\nu\frac{2L}{c}} = e^{i2\pi\frac{\nu}{\nu_{\mathrm{FSR}}}} = e^{i2\pi\frac{\Delta\nu}{\nu_{\mathrm{FSR}}}}$$

and thus $F(\nu)$ is a periodic function with a period of

$$\nu_{\mathrm{FSR}} = \frac{c}{2L}$$

which is called free spectral a range (FSR) and can be sufficiently described by the modulus frequency $\Delta\nu$.

The normalized intensity of the reflected beam as shown in fig. 3.3 is given by

$$|F(\nu)|^2 = 1 - \frac{(t^2)^2}{(1 - r^2)^2 + 4r^2 \sin^2 \frac{1}{2}\delta}$$

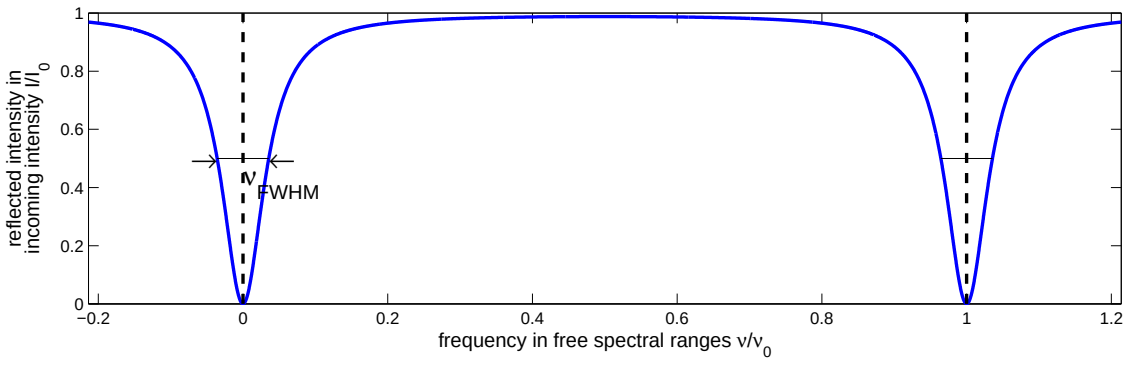

Figure 3.3: Normalized frequency spectrum of a Fabry–Pérot interferometer.

The FWHM for one of the intensity peaks computes by setting $\left|F(\frac{1}{2}\nu_{\mathrm{FWHM}})\right|^2 = \frac{1}{2}$ to

$$\nu_{\mathrm{FWHM}} = \nu_{\mathrm{FSR}} \frac{2}{\pi} \arcsin \sqrt{\frac{2t^4 - (1 - r^2)^2}{4r^2}} \approx \nu_{\mathrm{FSR}} \frac{2}{\pi} \arcsin \frac{1 - r^2}{2r} \approx \frac{\nu_{\mathrm{FSR}}}{\pi} \frac{1 - r^2}{r}$$

[4] not to be confused with the airy function.

The *finesse* $\mathcal{F}$ characterizes the width of the resonance relative to the free spectral range

$$\mathcal{F} = \frac{\nu_{\mathrm{FSR}}}{\nu_{\mathrm{FWHM}}} \approx \frac{\pi r}{1 - r^2}$$

3.1.3.2 A stable resonator

The presented Fabry–Pérot interferometer is on the border to instability, as only a perfectly collimated beam orthogonal to the surfaces would stay inside the interferometer for an infinite number of reflections and would guarantee perfect interference. This is why in practice curved mirrors are used to refocus the beam.

In such a resonator various spacial modes with similar frequencies can exist, and get populated depending on the parameters of the incoming beam. In most cases it is desired to excite the fundamental mode, which has a Gaussian intensity profile. The other modes are called **T**ransverse **E**lectro**M**agnetic modes, short TEM_{mn}- modes show m/n minima in their horizontal/vertical intensity profile and most importantly their phase ϕ develops differently in respect to the longitudinal z-coordinate (originating form the focal point) [20]

$$\phi_{mn}(z) = (m + n + 1) \arctan\left(\frac{\lambda z}{\pi w_0^2}\right)$$

where λ is the wavelength and w_0 the beam waist.

The simple model presented in sec. 3.1.3.1 still holds true, but the phaseshift δ for one "roundtrip" has to be replaced by twice the phase difference between the two mirrors, leading to a new resonance condition

$$\delta_{mn} = 2\left(\phi_{mn}(\text{Mirror 1}) - \phi_{mn}(\text{Mirror 2})\right) \stackrel{!}{=} 2\pi \cdot \boldsymbol{N} \tag{3.2}$$

This means that the spectrum of the resonator shows additional resonance frequencies that can be associated to a transverse mode with specific m and n. The relative strength of the TEM modes depends on the coupling to the incident exciting beam and its intensity profile.

3.1.4 Deriving the error signal

In order to achieve the necessary interference (as described in the previous section), sidebands are created by modulating the laser frequency. Fig. 3.4 shows how the laser beam is partly reflected of the resonator, separated from the incoming beam by a $\frac{\lambda}{4}$-plate and a polarizing beam splitter (PBS) and finally sent to a photodiode (PD) where the intensity of the interfering E-fields is converted to an electronic signal.

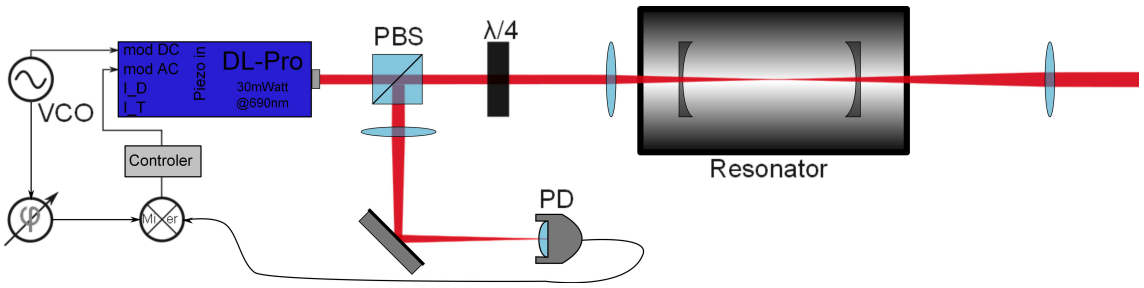

Figure 3.4: The optical setup for a PDH stabilization. A VCO modulates sidebands onto the laser, which propagates to the cavity, where it is reflected. The reflected beam is separated using a $\frac{\lambda}{4}$-plate and a polarizing beam splitter (PBS). The intensity is registered by a photodiode (PD).

The modulation can be achieved by using a Pockels cell, or by modulating the driving current for the laser diode. The phase-modulated field can be written as[5]

$$\begin{aligned} E(t) &= E_0 e^{2\pi i(\nu t + \beta sin\Omega t)} \\ &= E_0 \left[J_0(\beta) \mathrm{e}^{2\pi i \nu t} + J_1(\beta) \mathrm{e}^{2\pi i(\nu+\Omega)t} - J_1(\beta) \mathrm{e}^{2\pi i(\nu-\Omega)t} + \sum_{i>1} \left(J_i(\beta) \mathrm{e}^{2\pi i(\nu \pm \Omega)\mathrm{t}} \right) \right] \end{aligned}$$

where the $J_i(\beta)$ are the Bessel functions of the first kind, Ω the modulation frequency and β the modulation depth. For small modulation depths, the Bessel functions for orders $i > 1$ become very small and are of no significance in the following.

The laser spectrum (see fig. 3.5) thus consists mainly of the three frequencies ν, $\nu + \Omega$ and $\nu - \Omega$ with amplitudes $J_0(\beta)$, $J_1(\beta)$ and $-J_1(\beta)$. Note the minus sign indicating the sidebands being 180 degrees out of phase.

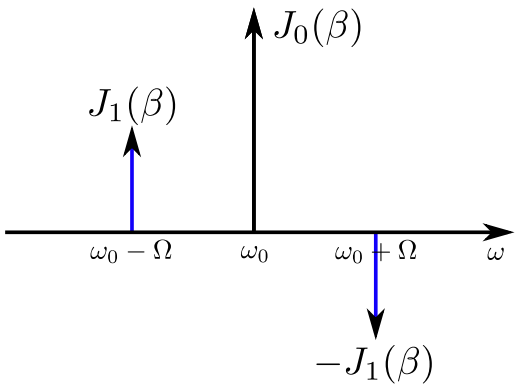

Figure 3.5: Sidebands created via frequency modulation.

The beam reflected from the resonator can be described by multiplying each fourier-amplitude with the corresponding frequency dependent complex reflection coefficient $F(\nu)$:

$$E_{refl}(t) = E_0 \left[F(\nu) J_0(\beta) \mathrm{e}^{2\pi i \nu t} + F(\nu+\Omega) J_1(\beta) \mathrm{e}^{2\pi i(\nu+\Omega)t} - F(\nu-\Omega) J_1(\beta) \mathrm{e}^{2\pi i(\nu-\Omega)t} \right] \tag{3.3}$$

The photodiode measures the resulting power which can be considered, for a certain resistance, as a voltage signal $U(t) \propto E_{relfl}(t)\overline{E_{relfl}(t)}$. Taking a look at the

[5] using the Jacobi-Anger expansion and $J_{-n}(x) = (-1)^n J_n(x)$

exponents in eq. 3.3 , reveals that the signal will consist of harmonic waves with frequencies 0 i.e. DC, Ω, and 2Ω. The phase information can be extracted from the Ω term, which computes to

$$U_\Omega(t) = |E_0|^2 J_1(\beta) J_0(\beta) \underbrace{\left[F(\nu+\Omega)\,\overline{F(\nu)} - F(\nu)\,\overline{F(\nu-\Omega)}\right]}_{A(\nu)} e^{2\pi i\,\Omega t} + \text{c.c.} \quad (3.4)$$

The frequency dependency within this equation is completely contained in the term abbreviated as $A(\nu)$. Since it is purely composed by the function describing the reflection coefficient, it inherits its periodicity and it is sufficient to consider $A(\Delta\nu)$.

The frequency information can now be extracted electronically by using a mixer, which is fed with the photodiode signal on one side, and on the other with the signal of the oscillator that generates the sidebands, delayed by a phase shifter. The output of this configuration can be expressed by

$$U_{\text{out}}(t) = U_{\text{in}}(t) \cdot \sin(\Omega t + \varphi_{\text{mix}}) = U_{\text{in}}(t) \cdot \frac{1}{2i}\left(e^{2\pi i\,\Omega t + i\varphi_{\text{mix}}} - \text{c.c.}\right)$$

Inserting the photodiode signal from eq. 3.4 yields

$$U_{\text{out}}(t) \propto \frac{1}{2i}\left(A(\Delta\nu)e^{2\pi i\,\Omega t} + \overline{A(\Delta\nu)}e^{-2\pi i\,\Omega t}\right)\left(e^{i\varphi_{\text{mix}}}e^{2\pi i\,\Omega t} - e^{-i\varphi_{\text{mix}}}e^{-2\pi i\,\Omega t}\right)$$

An additional low pass allows only the DC parts to pass, so the only terms that remain are the ones in which the exponentials cancel each other out, and the DC signal constitutes the error signal

$$\epsilon(t) \propto \frac{1}{2i}\left(A(\Delta\nu)e^{-i\varphi_{\text{mix}}} - \text{c.c.}\right) = \mathfrak{Im}\left[A(\Delta\nu)e^{-i\varphi_{\text{mix}}}\right]$$

Fig. 3.6 shows the theoretical error signal, computed for a reflection coefficient as derived in the previous section and a phase $\varphi_{\text{mix}} = 0$.

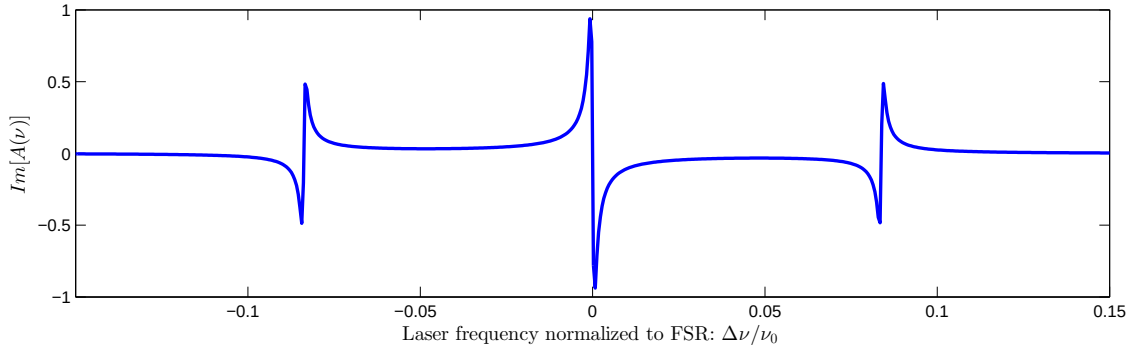

Figure 3.6: $\mathfrak{Im}\left[A(\Delta\nu)\right]$ for an optical resonator with a finesse of 6000 and a free spectral range of 1.5GHz.

There are three reasons for which ϵ is well suited as an error signal. First of all it exposes a very steep inclination around resonance ($\Delta\nu = 0$), secondly, the whole range of $(+\Omega, -\Omega)$ has the right sign for capturing a destabilized laser, and thirdly, the crucial central part can be well approximated by a linear relation between frequency deviation and signal strength.

For other phases φ_{mix} the inclination decreases until the signal becomes inverted. The reason for using the phase shifter is the necessity to compensate for a phase shift between the original oscillator and the signal arriving at the mixer, due to phase that it gathered while traveling the longer path from the laser to the diode and through the cables to the mixer.

3.1.5 Frequency discriminator

Finally $\mathfrak{Im}\left[A(\Delta\nu)e^{-i\varphi_{\text{mix}}}\right]$, which represents the error signal except for a scaling factor and possibly an offset, can be approximated in the case of an optical resonator with a resonance coefficient as described in sec. 3.1.3 in a region of the FWHM around a resonance as ([5])

$$\mathfrak{Im}\left[A(\Delta\nu)e^{-i\varphi_{\text{mix}}}\right] \approx -4\mathcal{F}\frac{\Delta\nu}{\nu_{\text{FSR}}} \tag{3.5}$$

This means that as long as the frequency deviations are small, there is a linear dependence between the error signal ϵ, which is measured in a voltage, and the current frequency deviation. The factor converting from the voltage domain to the frequency domain is called discriminator and defined as

$$d = \frac{\epsilon}{\Delta\nu}$$

so that the frequency deviation can be expressed as

$$\Delta\nu(t) = \frac{1}{d} \cdot \epsilon(t)$$

3.2 Measures for stability

To quantify the stability of our laser system we used the two measures that have been recommended by the IEEE for precision oscillators [33]. They are the Power Spectral Density as described in sec. 3.2.3 and the Allan Variance defined in sec. 3.2.4.

3.2.1 Basic definitions

The precision oscillator in our case is the electromagnetic field emitted by the laser diode and resonating within the cavity. The electrical field component can be described by

$$E(t) = E_0 e^{i(2\pi\nu_0 t + \varphi(t))} = E_0 e^{i\phi(t)} \tag{3.6}$$

Commonly the instantaneous angular frequency is defined as the derivative of the phase $\phi(t)$ of the exponential

$$\omega(t) = \frac{\mathrm{d}}{\mathrm{d}t}\left(2\pi\nu_0 t + \varphi(t)\right) = 2\pi\nu_0 + \dot{\varphi}(t)$$

As for a stable oscillator $\dot{\varphi}(t) \gg 2\pi\nu_0$, it is practical to define the dimensionless *fractional frequency*

$$y(t) = \frac{\omega(t) - 2\pi\nu_0}{2\pi\nu_0} = \frac{1}{2\pi\nu_0}\dot{\varphi}(t) \tag{3.7}$$

and analogously the *fractional phase*

$$x(t) = \frac{\varphi}{2\pi\nu_0}$$

They are related by the differential equation

$$y = \dot{x} \tag{3.8}$$

In the following it will be important to consider $y(t)$ as stationary, which is defined ([33] within [36])as:

> A random process is stationary if no translation of the time coordinate changes the probability distribution of the process.

3.2.2 Discretization and bandwidth limitations

For further processing of the error signal, it has been digitized, which means that there is a bandwidth limitation, which is determined by the acquisition device. A data point value y_k taken at a time $\tau_k = (k+1)/f_{\mathrm{DAQ}}$, where f_{DAQ} is the sampling frequency of the data acquisition device, can be modeled as

$$y_k = \frac{1}{\tau_0 - \tau_{\mathrm{Dead}}} \int_{\tau_k}^{\tau_k+\tau_0-\tau_{\mathrm{Dead}}} y(t)\mathrm{d}t \tag{3.9}$$

where τ_{Dead} is the dead time of the device.

This discretization acts as a low pass filter, which cuts off frequencies higher than the Nyquist frequency

$$f_h = \frac{1}{2} f_{\mathrm{DAQ}} = \frac{1}{2\tau_0}$$

since, according to the Nyquist–Shannon sampling theorem, oscillation at these frequencies cannot be reconstructed from the acquired y_k's.

There is also a bandwidth limitation f_l for low frequencies which is naturally given by the finite length of the measurement.

The mean frequencies for longer integration times $\tau_0' = n\tau_0$ ($n \in \boldsymbol{N}$) can be obtained by digitally averaging, after the data has been taken, n data points of a

acquisition with an integration time of τ_0, which means that we have a software control of the used bandwidth of acquisition. This has the advantage that less acquisition series have to be taken and thus the measuring process is accelerated and the data is easier to handle. Furthermore the additional acquired information can be of use, as will be explained later in sec. 3.2.4.

The increased data volume can be handled easily by modern computers. An acquisition rate of 1.5 MHz, corresponding to an integration time of 667ns, generates at double precision (64Bit), a data rate of 12 MBytes/s.

Discrete fourier transform For calculating the Power Spectral Density of frequency fluctuations (see sec. 3.2.3), it will be necessary to calculate the complex frequency component amplitudes A_m, which constitute the Fourier transform of the discrete y_k's. The discrete Fourier transform is defined as [26]

$$A_m = \frac{1}{N}\sum_{k=0}^{N-1} y_k e^{-2\pi i\, f_m \tau_k} = \frac{1}{N}\sum_{k=0}^{N-1} y_k e^{-2\pi i \frac{mk}{N}}$$

where the A_m's are associated with frequencies $f_m = m\Delta f$ for $m \in [0, N/2]$ and $\Delta f = \frac{1}{N\tau}$. The fact that the y_k's are real numbers yields

$$A_{N-m} = \overline{A_m}$$

3.2.3 Power spectral density

To characterize the frequency spectrum of a random signal, the Fourier transform (FT) is not sufficient, because itself is random a variable [31], which means that even for a stationary process the FT is time dependent. For this reason the power spectral density has been developed[6] (PSD) as a time independent measure of the probabilistic properties of a random signal. The PSD $S_y(\omega)$ of a signal $y(t)$ is defined as the power in the ω-frequency component carried by the signal.

Like every stochastic process, random signals can only be described within a limited certainty by a so called *estimator*. To obtain an estimator of the PSD one may use either an electronic device called a spectrum analyzer or compute it from a series of digitally acquired signal points. From the various estimators that exist, the *averaging periodogram* estimator is going to be used to characterize the noise signals. It is defined as

$$S_y(\omega) = \left\langle \left| \frac{1}{T}\int_0^T y(t)\mathrm{e}^{-i\omega t}\mathrm{d}t \right|^2 \right\rangle$$

where increasing times T and increasing numbers of terms contributing to the average improve the estimate.

[6] not to be confused with the spectral density.

Via the *Wiener Khintchine Theorem*

$$S_y(\omega) = \frac{1}{2\pi} \int_{-\infty}^{+\infty} g_y^{(1)}(\tau) \cdot e^{-i\omega\tau} \mathrm{d}\tau$$

the PSD can be related to the auto correlation of first order

$$g_y^{(1)}(\tau) = \left\langle \overline{y(t)} \cdot y(t+\tau) \right\rangle \tag{3.10}$$

The PSD also relates to the variance of the signal via

$$\int_0^\infty S_y(\omega) \mathrm{d}\omega = g_y^{(1)}(0) = \sigma_y^2$$

However the integral not necessarily converges for all signals, leading to a singularity in $g_y^{(1)}(0)$, which renders the estimation of a variance impossible. For this reason, definitions differing from the one above were developed.

3.2.4 Variances

There are several different types of variances that can be used to describe the data set of samples $\{y_k | k \in [1, N]\}$ with a mean of $\overline{y} = \frac{1}{N} \sum_{k=1}^{N} y_k$.

N-sample variance The N-sample variance, which is the "ordinary" variance, is defined as

$$\sigma_N^2 [y] = \frac{1}{N-1} \sum_{k=1}^{N} (y_k - \overline{y})^2$$

The fact that this variance does not always converge with $N \to \infty$, yields the necessity of other types of variances.

Allan-variance The Allan Variance is defined as

$$\sigma_A^2 [y_k] = \frac{1}{N-1} \sum_{k=1}^{N-1} \frac{1}{2} (y_{k+1} - y_k)^2 = \frac{1}{N-1} \sum_{k=1}^{N-1} \sigma_N^2 [y_i, i = k, k+1]$$

which is the average of variances of pairs, and is therefore also called *pair variance*. It is not subject to the same convergence problems as stated in [33]:

> ...it converges for all the major noise types observed in precision oscillators.

Modified Allan-variance The modified Allan-Variance (estimator[7]) is defined[30] as

$$\sigma^2_{\mathrm{modA}}\left[y_k\right](n\tau_0) = \frac{1}{2n^4(N-3n+2)} \sum_{j=0}^{N-3n+1} \left\{ \sum_{i=j}^{j+n-1} \sum_{k=i}^{i+n-1} \left(y_{k+n} - y_k\right) \right\}^2 \tag{3.11}$$

It was developed by D.W. Allan [1] to distinguish between white phase noise and flicker phase noise (cf. sec.3.2.5), which is not possible with the standard Allan variance (see formulas in tab. 3.1).

The modified Allan variance takes advantage of the additional information recorded when sampling at the highest frequency and deducing the lower bandwidth data in post-processing (cf. 3.2.2). Therefore eq. 3.11 includes additional sums.

3.2.5 Noise

A distinction between five major different types of noise has been developed empirically. These are considered independent and therefore the corresponding spectral densities can be added up. Each of them is characterized by a single parameter h_α indicating its prevalence. The total noise spectrum is given by

$$S_y(\nu) = \sum_{\alpha=-2}^{2} h_\alpha f^\alpha$$

Table 3.1 gives a summary of the properties of the different noise types.

Name	α	$S_y(\nu)$	$\sigma^2_A\left[y_k\right](\tau)$
White phase modulation	2	$h_2 f^2$	$\frac{3h_2 f_c}{8\pi}\,\tau^{-2}$
Flicker phase modulation	1	$h_1 f$	$\frac{3h_1 \ln(2\pi f_c \tau)}{4\pi^2}\,\tau^{-2}$
White frequency modulation	0	h_0	$\frac{1}{2}h_0\,\tau^{-1}$
Flicker frequency modulation	-1	$h_{-1}f^{-1}$	$2\ln(2)\;h_{-1}$
Random-walk frequency modulation	-2	$h_{-2}f^{-2}$	$\frac{1}{6}(2\pi)^2\,h_{-2}\,\tau$

Table 3.1: Citations of most common noise types in precision oscillators. f_c refers to the highest frequency that could be resolved.

3.2.6 Estimation of the laser linewidth

As the final goal of the stabilization is to reduce the bandwidth of the laser to the order of the linewidth of the ${}^1S_0 \rightarrow {}^3P_1$ transition to operate an efficient MOT, the quantity of interest is the linewidth of the laser. It can be deduced [7]from the

[7]for the full amount of data the calculation might take extremely long.

Allan-variance of the frequency fluctuations, if a Gaussian distribution of the y_k's is assumed, which means that the *characteristic function* is given by

$$\varphi_y(\tau) = \left\langle e^{2\pi i\nu\tau y} \right\rangle = e^{it\mu - \frac{1}{2}\sigma^2 t^2}$$

where μ is the mean value of y. The power spectral density $S_E(\omega)$ is calculated analogously to the spectral density of frequency fluctuations $S_y(\omega)$ using the Wiener Khintchine theorem. Therefore the auto correlation (eq. 3.10) of the electric field as defined in eq. 3.6 has to be calculated

$$g_E^{(1)}(\tau) = |E_0|^2 e^{2\pi i\nu\tau} \left\langle e^{i(\varphi(t+\tau)-\varphi(t))} \right\rangle_t \tag{3.12}$$

The phase difference in the exponent can be written with the normalized phase and by using the fundamental theorem of calculus and eq. 3.8 it can be related to the instantaneous frequency

$$2\pi\nu_0 \cdot [x(t+\tau) - x(t)] = 2\pi\nu_0 \int_t^{t+\tau} y(t')\mathrm{d}t'$$

where the integral over the frequency corresponds to the measured values y_k as defined in eq. 3.9. Hence the correlation function becomes

$$g_E^{(1)}(\tau) = |E_0|^2 e^{2\pi i\nu\tau} \left\langle e^{2\pi i\nu\tau y_k(\tau)} \right\rangle_t$$

Now the assumption of Gaussian distributed values sets in and resolves the correlation function to

$$g_E^{(1)}(\tau) = |E_0|^2 e^{2\pi i\nu\tau} e^{\pi\nu^2\tau^2\sigma_A^2[y_k](\tau)}$$

For an Allan-Variance that is predominantly due to white frequency noise and can thus be described by (see tab.3.1)

$$\sigma_A^2[y_k](\tau) = \frac{1}{2} h_0 \tau^{-1}$$

the power spectral density can be obtained analytically as

$$\frac{S_E(\omega)}{|E_0|^2} = \frac{1}{\pi} \frac{\gamma}{\gamma^2 + (\omega - \omega_0)^2}$$

which describe a Lorenz profile with a HWHM[8](in ω domain) of $\gamma = h_0\pi^2\nu_0^2$ which gives a FWHM[9] (in ν domain) of

$$\Gamma = h_0\pi\nu_0^2$$

[8] *H*alf *W*idth *H*alf *M*aximum
[9] *F*ull *W*idth *H*alf *M*aximum

3.3 Setup

The setup we realized on the optical table for conducting a PDH stabilization is straightforward and closely resembles the setup already shown in fig. 3.4. The complete optical setup, including the spectroscopy that will be discussed in chap. 5, is illustrated in fig. 3.7.

Following the propagation direction of the laser beam, starting from the diode laser, there is a sequence of a $\frac{\lambda}{2}$-plate and a polarizing beam splitter (PBS) to control the total intensity, and extract a fraction to couple it into a fiber and use it to measure the laser frequency with a wavemeter. In between the first PBS and the fiber coupler, there is another sequence of a $\frac{\lambda}{2}$-plate and a PBS, which could be used if light was needed for other purposes without disaligning the remaining setup.

Following the main path of the light, there is a lens system for mode matching the beam with the cavity (see sec. 3.3.3) and finally the PDH-setup as already described in sec. 3.1. Roughly 60% of the power of the stabilized laser passes through the cavity and is used for the spectroscopy)

3.3.1 Laser

As a laser source we use a TOPTICA DL-Pro system, which consists of an antireflection coated laser diode, emitting around 689nm, in Littrow configuration with an external tunable grating. Within the housing there also is an integrated Faraday isolator. The control system consist of a temperature control, a current control, a PDH unit, a fast analog control and a scan control. Fig 3.8 shows a scheme of the TOPTICA laser control system.

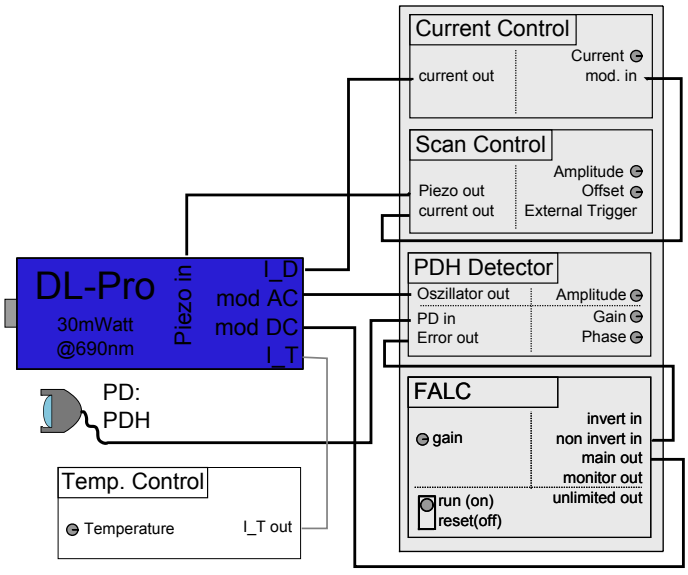

Figure 3.8: Scheme of control connections for the DL-Pro.

The control unit includes all necessary electronics for the PDH stabilization. The PDH detector consists of the oscillator that generates the sidebands at 20MHz, a mixer that is internally connected to it via a phase shifter and a low pass that extracts the DC information and provides the error signal at the error out port. For the input of the PDH photo diode, an amplifier is provided. There is also a controller unit (FALC), that offers various time constants for the internal series of extra slow limited integrator[10], slow limited integrator and fast limited differentiator. While their output is directly connected to the laser diode, there also is an unlimited integrator that connects to the scan control (controlling the piezo of the grating and the DC diode driving current) in order to compensate for drifts on a large timescale.

All connections are on a 50Ω basis. This implies that the total resistance, and therefore the saturation behavior, of the photo diode circuit is influenced by the PDH detector, such that the signal should only be monitored using a high impedance oscilloscope, when the PDH detector is connected. Also the connection between the PDH detector and the FALC has to be considered with care. Connecting a spectrum analyzer (50Ω) with a T-connector in parallel to the error out reduces the signal arriving at the FALC.

3.3.2 Resonator

As a cavity we used a commercial Advanced Thin Films (ATF) cavity of finesse 6000. It consists of two mirrors that are optically connected to a 10cm long spacer tube made of *ultra low expansion (ULE)* material manufactured by Corning. This material was chosen as it has a vanishing thermal expansion coefficient for a specific temperature. In our case this temperature has been measured by the manufacturer to be 35.9°C. Fig. 3.9 shows a plot of the temperature dependence of the thermal expansion coefficient.

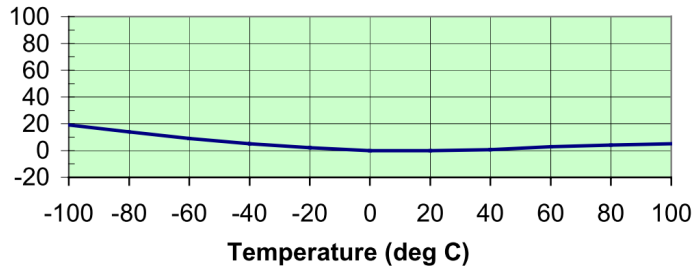

Figure 3.9: ULE expansion coefficient $\frac{\Delta L}{L}$ in [ppm] (y-axis) over temperature in °C[18].

[10]for control elements see [38]

3.3.2.1 Choice of mirrors

A decision had to be made whether to use a symmetric resonator with two curved mirrors with a radius of curvature of 50cm (ROC) facing each other, or to use an asymmetric resonator with one curved mirror (ROC=50cm) and a flat (ROC$\rightarrow \infty$) mirror. Since the two geometries imply different symmetries, the positions of the mirrors relative to the focal point in eq. 3.2 change. Therefore the distribution of TEM modes in the two cases is different. This is important, even though for the stabilization only the fundamental mode is going to be used, because in most cases the beam that has to be coupled into the resonator is not perfectly Gaussian shaped. It may for example have a slightly oval cross section causing transverse modes to be excited, even though the focal point, divergence and incident angle might have been adjusted perfectly. This is not desired, since they possibly modify the reflection coefficient (eq. 3.1) in such a way that it disturbs the locking scheme.

To estimate the position of the transverse modes consider the two resonance conditions [20] for the different geometries

$$\frac{\nu}{\nu_{\mathrm{FSR}}} = (q+1) + c_s(m+n+1)$$

with q being an integer number, corresponding to the order of the axial modes, m and n as defined before (sec. 3.1.3) and c_s a constant defined by the geometry

$$c_{(\ )} = \frac{1}{\pi}\arccos\left(\mathrm{sgn}\left(1-\frac{L}{\mathrm{ROC}}\right)\sqrt{1-\frac{L}{\mathrm{ROC}}}\right)$$
$$c_{(\,|\,} = \frac{1}{\pi}\arccos\left(1-\frac{L}{\mathrm{ROC}}\right)$$

The occupation of the different TEM modes depends on the intensity profile of the incident beam. It can be determined by projecting the intensity profile onto the basis that is formed by the set of profiles associated to the TEM modes. Generally the higher order TEM modes are more difficult to excite. More likely to excite are the lower TEM modes as for example by an aspect ratio of a Gaussian beam different from one.

Therefore for the best operation of a PDH-lock, the lower order TEM modes around the Gaussian modes should be maximally suppressed.

Lets consider a specific fundamental mode with $q = Q$, then all the lower lying modes with $q = Q - q_\Delta$, where $q_\Delta \in \{1, 2, ..., Q\}$, will have equidistant TEM-modes at higher frequencies, possibly close to the one of the one of the fundamental mode with $q = Q$. The frequencies of these q_Δ modes relative to the Q mode are given by

$$\Delta\nu = \frac{\nu_{q_\Delta nm}}{\nu_{\mathrm{FSR}}} - \frac{\nu_{Q00}}{\nu_{\mathrm{FSR}}} = -q_\Delta + c_s(m+n)$$

If we define a window of interest of $\pm\nu_w = \pm 30\text{MHz}$, which is necessary for a PDH stabilization with sidebands of 20MHz, around the fundamental mode Q, we can formulate the problem as follows

$$\frac{\nu_w}{\nu_{FSR}} < \Delta\nu < \frac{-\nu_w}{\nu_{FSR}}$$

which is equivalent to

$$\min\left\{q_\Delta \mid \left(q_\Delta + \frac{\nu_w}{\nu_{FSR}}\right) \mathrm{mod} c_s < 2\frac{\nu_w}{\nu_{FSR}}\right\}$$

This means we find the smallest q_Δ for which a TEM mode exists that falls into the 30MHz window.

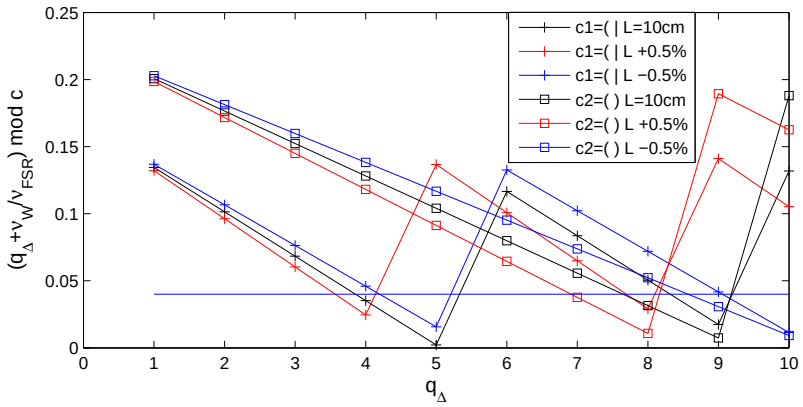

Figure 3.10: TEM modes for two different resonator types: + indicates an asymmetric and □ a symmetric resonator. The y-axis corresponds to the normalized frequency difference between a resonance of order Q and the TEM modes corresponding to a lower order $Q - q_\Delta$ where the blue line indicates the window of ±30MHz to be kept clear. The symmetrical resonator shows to be the better choice.

In fig. 3.10 the problem is solved graphically. The lines with the squares represent the double concave resonator, while the crosses correspond to the asymmetrical concave-plane resonator. There are three lines for every configuration: the central one for a mirror distance of 10cm, the lower and upper for a slightly different length of $\pm 0.5\%$. The horizontal solid blue line represents the window around the fundamental resonance. For points below that line, a TEM mode exists within the specified window. The graphic shows clearly that the symmetric cavity should be used.

3.3.2.2 Housing

The cavity is mounted within a special housing produced by Stable Laser Systems. The housing ensures that the exact temperature of the zero crossing of the thermal expansion coefficient is maintained by thermal isolation/shielding and a heating resistor, that we controlled with a temperature control that was build by our electronic workshop. The input for this control is an integrated type F thermo resistor. Furthermore the housing provides vibrational isolation and can be evacuated in order to avoid frequency fluctuations caused by atmospheric pressure changes, which change the optical density of the air between the mirrors.

3.3.3 Mode matching

To transfer the maximum power into the fundamental mode, the incident beam has to be adjusted in such a way, as if it was the extension of that mode. There are six beam parameters, if we assume the incident beam to be Gaussian: position of focus (3x), angle to focus (2x) and divergence (1x), which is equivalent to the beam waist. Four of those, angle (2x) and the position of the focus within the plane perpendicular to the propagation direction (2x), can be adjusted by using a pair of mirror mounts. The remaining two are determined by a lens system.

Since the cavity within the housing has an optical axis that is well above the beam level used in the rest of the experiment, an elevator, constructed from two parallel mirrors, located right in front of the housing, lifts the beam axis to match the one of the resonator. It also serves well for fine tuning the coupling because the two mirrors it is made of are the ones closest to the resonator and hence offer the highest precision.

3.3.3.1 Lens system

The lens system we used consists of a focusing lens of 500mm focal length, located on a translation stage at a beam distance of 500mm from the center of the cavity to create the right focal point for a collimated beam, and a telescope right before this lens to ensure a beam diameter that results in the desired divergence for the used focal length of the focusing lens.

To calculate the divergence we consider, as described in the previous section, the boundary conditions of the Gaussian beam, which are given by the mirror pair

forming the cavity. The radius of curvature (ROC) R of a Gaussian beam with waist w_0 and wavelength λ at a distance z from the focus is given by [19]

$$R(z) = z\left[1 + \left(\frac{\pi w_0^2}{\lambda z}\right)^2\right]$$

This allows to express the necessary beam waist for a cavity of length L and two mirrors of ROC R as follows

$$w_0 = \sqrt[4]{L(2R - L)\left(\frac{\lambda}{2\pi}\right)^2}$$

For $R = 50\text{cm}$ and $L = 10\text{cm}$ the waist has a radius of

$$w_0 = 181\mu\text{m}$$

and leads to an asymptotic divergence of the beam of

$$\theta = 1.2 \cdot 10^{-3}\ \text{rad}$$

At a distance of 500mm, at the focusing length, the beam has widened to a radius of

$$w_{\text{Lens}} = 600\mu\text{m}$$

The beam that is emitted by the DL-Pro is only slightly divergent. The radius at a distance equal to the distance of the first lens of the telescope, has been measured with a razor blade mounted on a micrometer table to determine the integrated power profile.

$$w_{\text{DL-Pro}} \approx 400\mu\text{m}$$

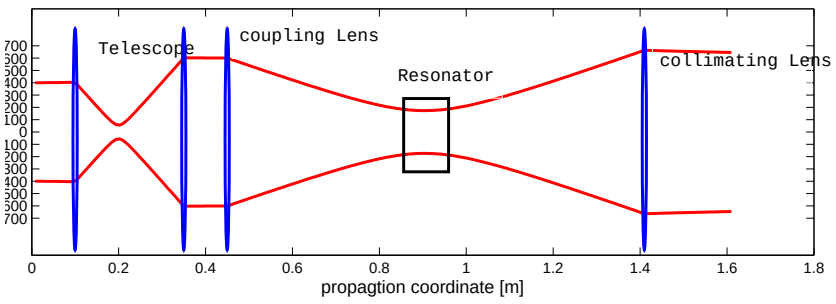

Figure 3.11: Scheme of the beam profile for mode matching the resonator.

The ratio of 2:3 simplifies the choice of lenses for the telescope. We chose a 100mm lens and a 150mm lens. The beam shape is illustrated in fig. 3.11.

3.3.3.2 Mode matching process

During the course of the experiment the cavity had to be taken out of the optical system a few times. In the following, the sequence that evolved for matching the beam parameters most quickly will be outlined.

As preparation, it is recommendable to measure the cavity position relative to the housing and mark the focal point on the housing.

- At first the beam should be aligned, without the cavity, so that it is at the right height and parallel to a table edge.
- The focus of the beam should be found to set the housing in place so that the mark is situated at the focus and it is also parallel to the table.
- Then, using full intensity and scanning the laser over a FSR or more, the beam should be aligned roughly via the two mirrors in front of the cavity. When positioning the beam into the center of the housing entry (via the mirror first hit by the beam), a weak transmission should already be observable[11]. Usually it looks like two fuzzy points with ring like structures. The points should be brought to maximum overlap to minimize the size of the pattern.
- Once the pattern is minimized, the frequency scan can be turned off or reduced to a very low amplitude. Now, manually tuning the frequency the fundamental Gaussian mode can be found.
- Increasing the scan a little, the transmission peak can be displayed using a photodiode and can be maximized by a beam walk.

[11] The room light should be shut off.

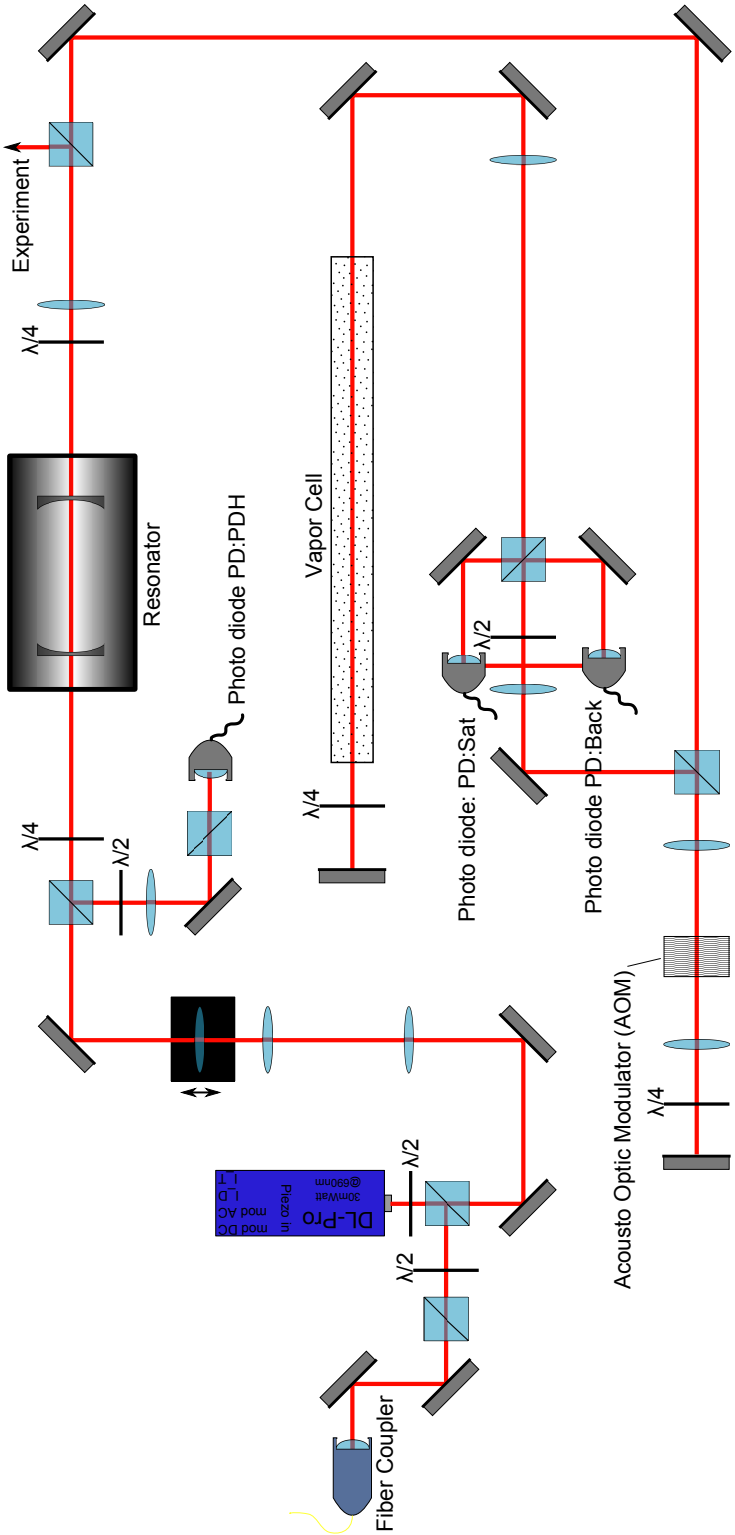

Figure 3.7: The complete optical setup for the laser stabilization.

4 Characterization of the relative frequency stability

4.1 Preadjustments

To lock the laser, it is set to scan over the desired resonance. First the coupling to the cavity was improved by adjusting the two elevator mirrors while monitoring the reflection signal on the photodiode PD:PDH as shown in fig. 3.7. Then, the lambda plates angles were adjusted to attain the most profound dip possible.

Next the error signal was monitored using a 1.5MHz low pass filter. By varying the phase delay and the lambda plates, it was adjusted in such a way to resemble most closely the ideal signal $A(\nu)$ (fig. 3.6).

4.1.1 Discriminator

To determine the discriminator it is not possible to scan the laser over a resonance, record the error signal and fit a straight line around the center, because the free running laser is not stable enough to resolve the steep slope. Fig. 4.1 shows one of the best results for an error signal. The black line is the raw data, the blue line shows the data processed by a digital low pass and the red line was obtained by manually fitting a theoretical curve.

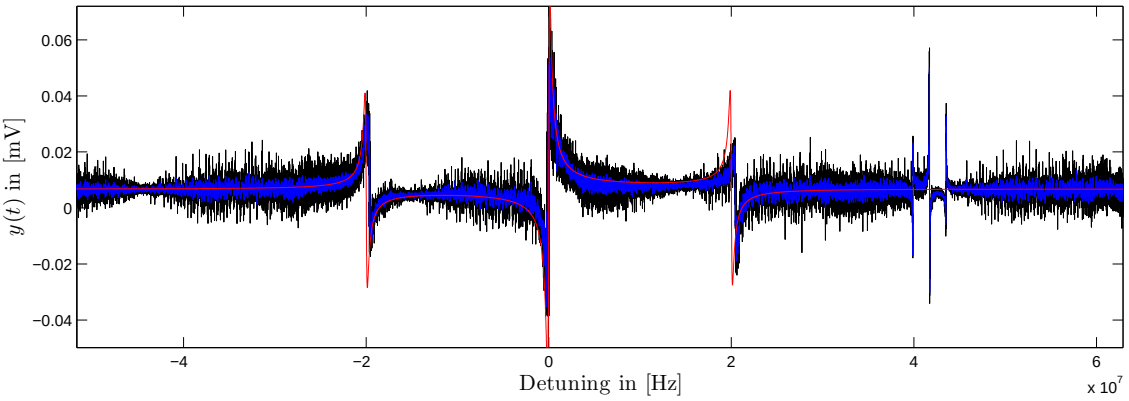

Figure 4.1: Error signal, taken with a free running laser (black), after digital low pass of 1.5MHz (blue) and theoretical curve (red).

For the fitting we trusted the finesse of 6000 that was measured by the manufacturer. Taking the maximum and minimum values of this signal, creates a scale for $A(\nu)$, thus we can describe the error signal ϵ by

$$\epsilon(\Delta\nu) = \frac{(\max\epsilon - \min\epsilon)}{2} \cdot \mathfrak{Im}\left[A(\Delta\nu)e^{-i\varphi_{\mathrm{mix}}}\right] + \epsilon_{\mathrm{offset}}$$

Eq. 3.5 yields for the current frequency

$$\Delta\nu(\epsilon) = -\frac{\nu_{\mathrm{FSR}}}{2\mathcal{F}} \frac{\epsilon - \epsilon_{\mathrm{offset}}}{(\max\epsilon - \min\epsilon)}$$

The fractional frequency $y(t)$ as defined in eq. 3.7 can then totally be described by the error signal

$$y(t) = \frac{\Delta\nu(\epsilon(\mathrm{t}))}{\nu_0} = -\frac{\nu_{\mathrm{FSR}}}{2\mathcal{F}\nu_0\,(\max\epsilon - \min\epsilon)}\,(\epsilon(t) - \epsilon_{\mathrm{offset}})$$

Before taking any stability measurements, a series of discriminator signals were recorded to determine the corresponding discriminator from the distance of the extrema for each scan.

Once this was achieved, the standard settings for the FALC were activated and the gain maximized to correct the offset. Reducing the gain to zero again, the scan amplitude was reduced as much as possible without losing the resonance. By slowly increasing the gain the laser was locked. Once it was locked, the scan was turned off and the unlimited integrator turned on and adjusted to keep the error signal without offset.

The noise of the reflected signal on the PD:PDH was minimized by trying various settings for the FALC and repeating the whole process with different PDD settings if necessary.

The resulting descriminator values can be found in tab. 4.1 in the following section.

4.2 Measurement series

To measure the frequency fluctuations of the laser relative to the cavity, the error signal of the locked and preadjusted laser was recorded with the acquisition card, which has a high impedance and does not extract power from the signal. One billion points were recorded at a frequency of 1.5MHz for various sets of filter settings, light powers on the PDH-diode and couplings as listed in tab. 4.1.

The further analysis of stability, computing the Allan variance and PSD, was conducted in post processing. To operate on comparable values, the data has first been converted to normalized frequency deviations as described in the preceding section.

4.3 Power spectral density

The power spectral density of the normalized frequency fluctuations was computed for five different data sets by the averaging periodogram method (see sec. 3.2.3) and

No	1	2	3	4	5
Power before cavity [mW]	5.5	7.77	8.34	13.1	12.5
Power after cavity [mW]	2.75	4.56	4.12	7.03	6.58
Laser diode current [mA]	658	643	643	587	589
Laser diode temperature [°C]	23.6	23.6	23.6	23.6	23.6
Grating piezo	9.28	9.52	9.40	6.32	6.28
PDD sideband amplitude	4	5	5	2	2
PDD gain	7	max	max	8	8
PDD phase	0	0.5	0.1	0.4	0.4
Unlimited integrator	0	0	0	0	0
Extra slow integrator	5	5	5	5	5
Slow integrator	5	5	5	5	5
fast limited differentiator	10	10	10	10	10
Prop. gain [in deg, start at 6 o'clock]	-	50	55	90	90
Invert/non-invert	non	non	non	non	non
Air pressure in cavity [mBar]	10^{-2}	0.61	57	60	room
Temperatrue [°C]	25	25	25	25	25
Discriminator $\left[\frac{\text{mV}}{\text{kHz}}\right]$	-0.369	-0.805	-1.111	-0.138	-0.152

Table 4.1: Settings for the different measurements.

plotted in double logarithmic scaling in fig. 4.2. To achieve a good resolution in the logarithmic scale without having to Fourier transform the complete set of 8 GB worth of data, the bandwidth was reduced to various values by averaging. The red dashed lines indicate the limits between regions that rely on different bandwidths. There are three bandwidth regions per decade with 2^{15} points each, each being divided into 32 averaging samples of 1024 points.

By only considering an interval finite in time, a leakage error is introduced. This means that some of the energy belonging to a certain frequency leaks into the bins of neighboring energies. The effect can be made plausible by imagining the available data as a product of the infinite data stream with a rectangular function. The Fourier transform thus is the convolution of the rectangular function with the transform of the infinite signal. To reduce this effect a hamming window[31] was applied by multiplying every of the N points with a window function value $w(k)$ corresponding to its index k

$$w(k) = 0.54 - 0.46 \cos\left(\frac{2\pi k}{N-1}\right)$$

The Fourier transform of this window has less side lobes than the one for the rectangular one and therefore causes a smaller leakage. Applying a window also reduces the amplitude of the resulting signal, for which it has to be compensated by a *process loss factor*, which in case of the Hamming window has a value of 0.4.

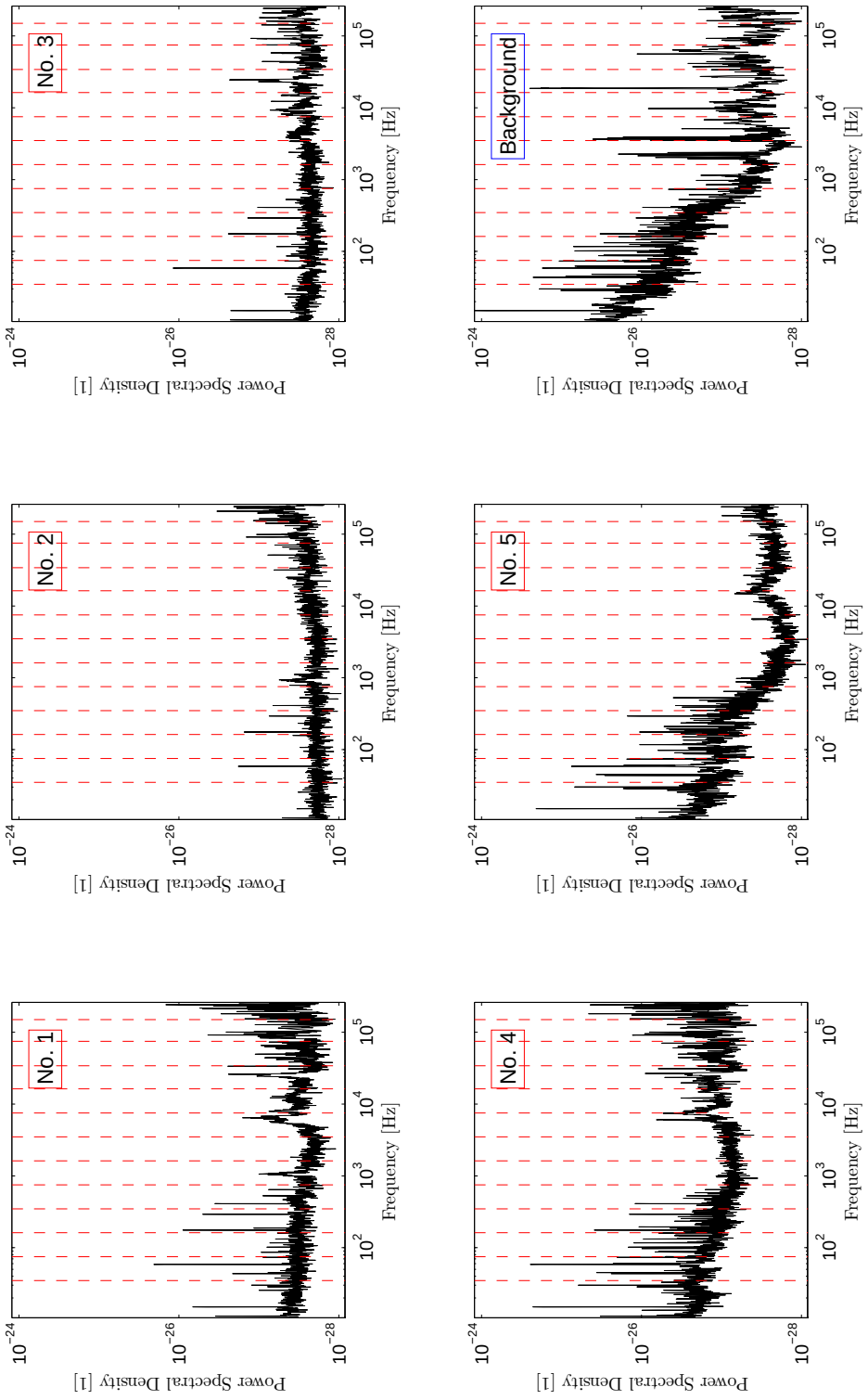

Figure 4.2: PSD for the five measurement series and the background signal for a null PD input.

The last frame shows the background spectrum, where background refers to the error signal produced if the laser beam is blocked in front of the PD:PDH. Since there is no discriminator to be assigned to this signal, it is scaled with the discriminator of series no. 5 for comparsion.

The first three measurements are dominated by white frequency noise, while the last two show increased noise going towards lower frequencies. While recording the scanned error signals to determine the discriminator, it was already obvious that the amplitude of the electronic background noise was close to the amplitude of the error signal itself. Interpreting the discriminator value[1] as the relative strength of the error signal vs. the noise is corroborated by the increasing low frequency noise for signals with decreasing discriminator, i. e. the noise dominated over the error signal as it can be clearly seen by comparing the last two frames that are at the same scale. Nevertheless it is interesting to see how the stabilization could compensate quite a bit of that electronic noise, especially in the high frequency regime.

The smaller discriminator values principally originate in the smaller sideband amplitudes that have been chosen while optimizing the PD:PDH signal as shown on an oscilloscope. There, amplitudes of around two[2] seemed to deliver the best results. A main source for the background noise is the acquisition card or computer itself. When connecting the acquisition card to the error out, or even only the computer to the energy line, the signal significantly deteriorated. This indicates a problem with ground loops. Therefore the ground connections were optimized but the problem remained. An energy line filtering system, might solve the problem by using high capacity batteries to minimizing the impact of the noise the computer feeds back via its power supply. The implementation of such a system is already planned.

For the data taken only the first three series can be considered as an estimate. All spectra show the strongest or second strongest peak at 58.4 Hz, probably caused by the energy network with a specified frequency of 60Hz. Also the second, fourth and sixth harmonics appear. The first two measurements additionally show a broader band of noise around 1000 Hz. The least noisy spectra are no. 2 and 3, where no. 2 seems to show a slightly increasing noise level for the high frequency limit.

4.4 Allan variance and laser linewidth

The normal Allan deviation was calculated for logarithmically spaced timescales with a density of 20 timescales per decade. The averaging factor was chosen as 100. The result is shown in a double logarithmic plot in fig. 4.3 (black line).

[1] The discriminator value scales the error signal. Strong sidebands for example lead to a strong error signal. When the laser is scanned over resonance the maximum and minimum peak determine the discriminator value.

[2] on the internal scale of theToptica PDD detector.

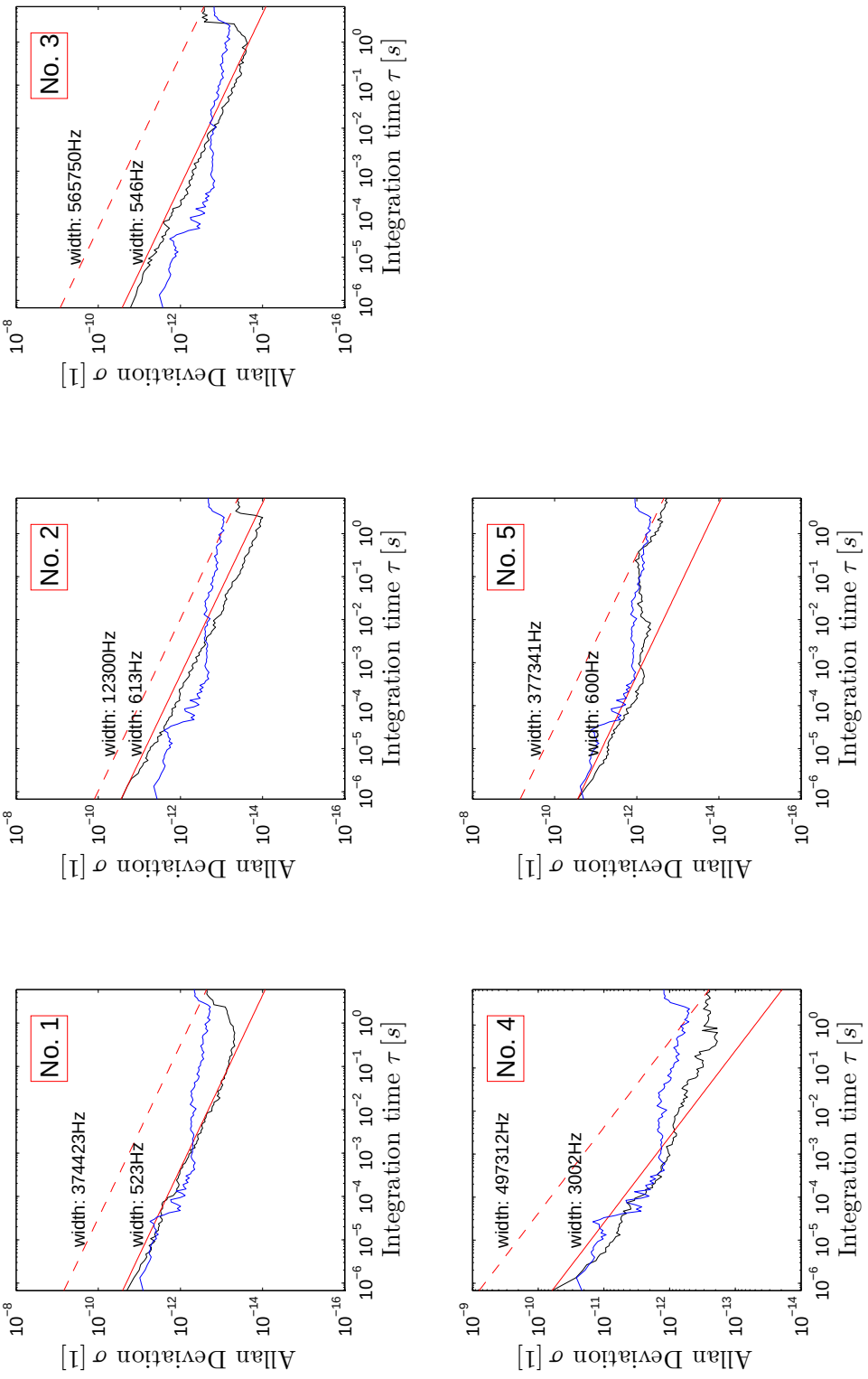

Figure 4.3: Allan deviation σ for various different configurations of the system. The deviation is plotted in black over different integration times τ. The straight lines represent the Allan deviations of power spectra with Lorentz profiles of a FWHM as indicated. The corresponding noise is white Frequency noise. The blue line represents the background noise of the data acquisition card, scaled accordingly to the measured signal.

The blue line shows the background noise scaled with the corresponding discriminator for each sample. The two red lines show the theoretical Allan deviation for perfectly white frequency noise, which is (see tab. 3.1) proportional to $\tau^{-\frac{1}{2}}$ and appears in a double log plot as a line with an inclination of $-\frac{1}{2}$. The y intercept is chosen as such, that the dashed line is an upper limit for the variances on all timescales and the solid line is an upper limit neglecting the very long time scales.

In concordance with the PSD considerations, the first three measurements show closest resemblance to white frequency noise, while the last two deviate strongly and show the strongest influence by the background noise. All measurements show a harsh increase of noise for timescales longer than one second. This noise was already visible on the oscilloscope when making the preadjustments, if the control computer was connected. The fact that it also appears in the background means that it is of electronic origin. Again a energy line filtering system might solve the problem.

To each ideal line of Allan deviation, the corresponding laser linewidth has been calculated as described in sec. 3.2.6. Neglecting those low frequency instabilities, a laser linewidth of the order of 500 to 600 Hz has been achieved for the first three series, which fulfills the exigence of a stability better than 1kHz.

5 Spectroscopy as an absolute frequency reference

5.1 Optical setup

The optical setup is shown in fig. 3.7 as a part of the complete laser setup. Once the laser is locked to the cavity ca. 60% of the incoming intensity are transmitted and the setup for the spectroscopy can be aligned.

Right after the cavity the beam is collimated by a 500mm lens to an $\frac{1}{e^2}$-diameter of 600µm. A $\frac{\lambda}{4}$-plate converts the transmitted circularly polarized light into linearly polarized light with such a polarization axis orientation that a desired fraction is split off by a polarizing beam splitter and can be used for the main experiment, while the remaining fraction is guided by two mirrors and an elevator to the double pass AOM setup as shown in detail in fig. 5.1.

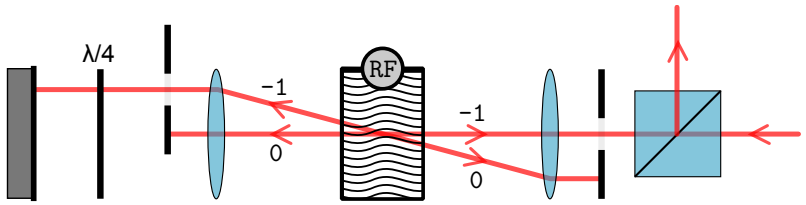

Figure 5.1: Schematic illustration of the double pass configuration. The AOM is situated in the focus of a telescope, and the -1^{st} order of diffraction is used twice to control the field frequency, without changing the beam parameters.

To guide a beam in double pass configuration through an AOM, the AOM is placed within the focus of a 1:1 telescope[1]. A mirror behind that telescope, forming a right angle with the beam axis, reflects both, the deviated and unperturbed beam, back into themselves as the change of the $\overrightarrow{k}$-vector by the AOM in the focal point is translated by the telescope lens to a parallel displacement. In the second pass the deviated beam is deviated once again by the same amount into the opposite direction, as it is now entering from the other side, and overlaps with the incident beam as well as with the beam that has not been deviated during both passings.

We want to isolate the beam that has been deviated twice. This is achieved by an iris that blocks the zeroth order in each direction, and a $\frac{\lambda}{4}$-plate in combination with a polarizing beam splitter. The frequency of the field of the resulting beam can now be changed by the AOM without changing the beam parameters, which allows to make a scan without destroying the beam overlap of the saturating and probing beam required for the saturation spectroscopy.

[1] two lenses with the same focal length f with a distance of $2f$.

From there on a telescope can be inserted to enlarge the beam diameter in order to reduce the transient broadening (see sec. 6.2.3). Between the lenses of the telescope, there is a $\frac{\lambda}{2}$-plate and a polarizing beam splitter to extract some power from the main beam and measure it with the photodiode PD:Back in order to determine the power fluctuations caused by the frequency dependent performance of the AOM.

The widened beam passes through the cell twice, first as a pump beam, and then being reflected from a partially transparent mirror that reduces its power by 75%, and once as a probe beam, with polarization axis rotated by 90° by passing a $\frac{\lambda}{4}$-plate twice, so that it will separate from the pump beam at the PBS and fall into PD:Sat.

5.2 Spectroscopy cell

For conducting saturation spectroscopy[2] on the ${}^1S_0 \rightarrow {}^3P_1$ line of strontium, one has to take into account some element specific properties, such as the vapor pressure and the small cross section, which demand high temperatures, or the window coating properties, which demand a setup that protects the windows. Following the design ideas by Ferrari et al. [14] and Simon Stellmer we managed to build a spectroscopy cell that allowed us to successfully observe the Lamb dip.

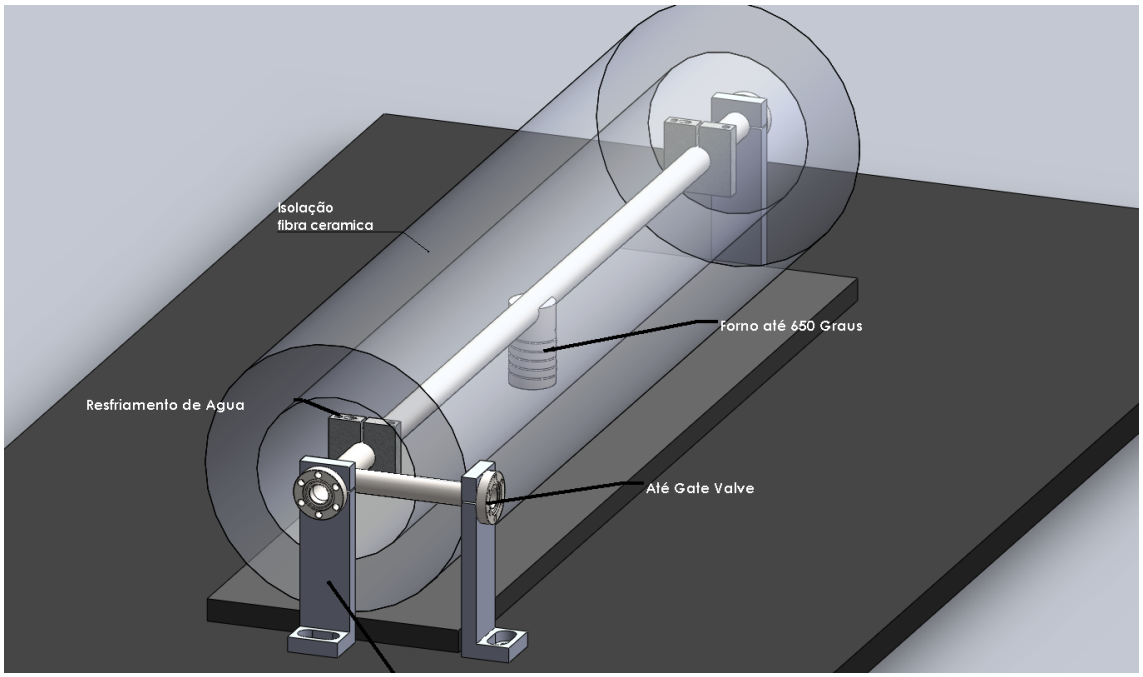

Figure 5.2: Illustration of the CAD model for the spectroscopy cell.

[2]for a discussion of saturation spectroscopy see for example [10].

Fig. 5.2 shows an illustration of the CAD model of this spectroscopy cell. It consists principally of a tube of 750mm length and 19mm/16mm outer/inner diameter, with an oven attached to its center. The oven has an inner/outer diameter of 26mm/30mm and extends 45mm from the main axis of the tube to its bottom, plus 6mm for an extra thick wall, in which a hole is drilled to place a thermocouple for monitoring the oven temperature.

The heating is achieved by an isolated resistor wire with a total diameter of 1mm, 600mm length and an approximate resistance of 5Ω. To improve the thermal contact and facilitate the mounting, guiding lanes have been cut into the oven wall. They have a semicircular cross section and follow a double spiral path which has three windings each. To mount the wire, it was bent in the middle so that the two ends could be wound simultaneously over the double spiral. This geometry allows to minimize the magnetic field induced by the heating current.

The thermal isolation was achieved by using the ceramic fiber material *thermalblanket H10*[3] which endures up to 1260°C. We wound several layers around the central section and fixed it using screw clamps. To protect the optics and lungs from particles and strings of the fiber material and provide some further isolation, a few more layers of aluminum foil were added.

For contacting the heating wire, the ends were led to opposing sides, and only after a first layer of fiber isolation, they were connected using terminal connectors (without plastic housing), as solder and heat shrink tubes do not resist the required temperatures.

Additional cooling blocks were mounted on the main tube. They provide the possibility for water cooling. It turned out that the temperature drops quickly in short distances from the oven and thus the water cooling was not used and the isolation was only required for the central third.

For optical access MDC CF16 viewports were used. For maximum intensity they were anti reflection coated from the outsides in the optical workshop of the IFSC. In order to separate the remaining reflex from the beam, they were mounted under a small skew angle.

To control the pressure, another tube was soldered in a right angle to the main tube and connected via a CF16 flange to another T at which a Pirani guage was attached to measure the pressure. The remaining opening was connected to a valve and provides access for pumping and filling with a buffer gas.

The whole construction is held by three aluminum supports at an axis height of 17.5cm. Care has to be taken with the imbalance caused by heavy vacuum connections.

[3] www.perfiltermico.com.br

5.2.1 Estimation of Parameters

In order to achieve an operational cell with minimum line broadening some parameters had to be estimated. These are the diameter for allowing a beam that minimizes transient broadening and a length that protects the windows from being coated at a certain buffer gas pressure for minimal collisional broadening.

5.2.1.1 Diameter

The velocity distribution for an ideal gas is described by the Maxwell-Boltzmann distribution as described in sec. 2.1.3 At a temperature of $T = 500°\mathrm{C}$ the mean velocity is

$$\bar{v} = 442\frac{\mathrm{m}}{\mathrm{s}}$$

For a linewidth of 7.6kHz the traveled distance in the excited state results in

$$d_{\mathrm{exc}} = 9.2\mathrm{mm}$$

If any smaller beam is used transient broadening takes place (see sec.6.2.3).

5.2.1.2 Pressure

For the pressure chosen for the spectroscopy cell, there is an upper and lower limit. It must not be to high, which would lead to collisional broadening (for a more detailed treatment see sec. 6.2.2), and it must not be to low which would lead to a rapid coating of the windows.

To estimate the upper limit, consider the mean free path of an strontium atom within an argon buffer gas of partial pressure p

$$l_{\mathrm{MFP}} = \frac{1}{\sigma n} = \frac{1}{\pi d^2}\frac{k_{\mathrm{B}}T}{p}$$

where d is the sum of the atomic radii, which defines a simple cross section $\sigma = \pi d^2$. n is the atomic density derived from the equation of state of an ideal gas (compare eq. 2.1). In case of strontium and argon, the atomic radii are [2]

$$r_{Ar} = 71\mathrm{pm}$$

$$r_{Sr} = 200\mathrm{pm}$$

and for a $l_{\mathrm{MFP}} > d_{\mathrm{exc}}$ lead to an upper pressure limit of

$$p_{\mathrm{lim}} < 2 \cdot 10^{-3}\mathrm{mBar}$$

To calculate the pressure at room temperature, one may apply the equation of state of an ideal gas, which states the proportionality of p and T for a fixed gas density. Thus the pressure while filling must be about a third lower than the one aimed for.

These considerations neglect the collisions of strontium atoms with strontium atoms, which can only be controlled by varying the temperature of the cell, which can only be done within a small window, as for a satisfactory spectroscopy signal a certain partial pressure of strontium is necessary.

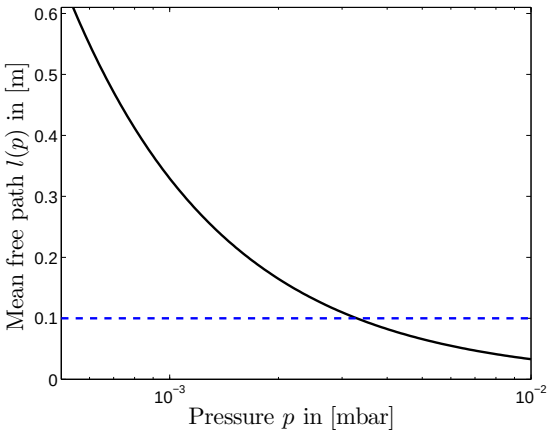

Figure 5.3: The pressure dependence of the mean free path of strontium vapor at 500°C in argon buffer Gas. The blue line indicates the distance an excited strontium travels in average before decaying.

5.2.2 Filling the oven

The filling procedure was quite cumbersome, since strontium is relatively hard, requires a protection atmosphere and sticks to the steel of the cell.

Due to the tubes length we needed to construct a housing for the protection atmosphere. As a buffer gas we used argon, which we fed under constant flux into the housing.

Because of the hardness of the material, cutting the strontium inside the atmosphere turned out to be more difficult than assumed. The use of a small electrical power tool is highly recommended. Despite the argon atmosphere, the strontium starts oxidizing during the filing process. However this did not cause any problems so far.

Care has to be taken in guiding the strontium to the oven, since bigger chunks get stuck easily and smaller ones might remain in the main tube and eventually might find their way to the windows or pumping system. Therefore one has to be constantly aware of not tilting the apparatus more than a few degrees.

Once the oven was filled, we pumped and baked at ca. 80°C for several days to evaporate all impurities. Afterwards we used two valves to alternatingly flood it with argon and evacuate to minimize the amount of impurities and air in the vicinities of the connector parts, such as valves and pressure gauges, that were not baked. In the end we slowly let argon into the cell and closed the valve as we reached a pressure of 10^{-3}mBar at room temperature. The use of a buffer gas is crucial to prevent the

strontium from coating the windows, which would take less than an hour[4] without any buffer gas.

5.2.3 Improvements

There are several improvements that could be implemented for building another cell. For example a little hook soldered or screwed to the side of the oven cylinder, to hold the bent center part of the heating wire right in place where the double spiral ends and thus facilitating the mounting of the heating wire. It would also be handy to have some high temperature material at hand to fix the wire to its position inside the lanes.

Concerning the vacuum connection, it would save space on the optical table if the connection would be pointing upwards.

It would be easier if the T for connecting the gauge would be included as one piece. It could be covered by a blind flange if no gauge is needed.

It would be worth thinking about attaching an extra tube for accessing the oven from above, so that filling in strontium would become easier and if parts got stuck they would not block the optical access and would not stick to the windows.

5.3 Laser system locked at atomic resonance

In the final setup the laser frequency will be fixed by the resonance frequency of the cavity to which it will be locked. The choice of the cavity mode is free, however, the frequency of the chosen cavity mode can not be tuned further. The range in which the laser frequency can be scanned will be restricted by the AOM bandwidth which is generally much less than 1GHz and thus smaller than than one FSR (≈ 1.5GHz) of the reference cavity. Therefore we needed to determine the right resonance to which to lock, i.e. the closest one to the atomic resonance, and to chose the right type and diffraction order ($\pm$) for the AOM to bridge the gap.

To achieve this we set up a preliminary saturation spectroscopy, using the beam from the PBS before the fiber coupler (c.f. fig. 3.7) with almost full intensity to obtain a well power-broadened lamb dip. With the remaining intensity we monitored the power reflected from the cavity into PD:PDH.

Using the wavemeter for comparing against the literature [14] value of

$$\nu_0 = 434\ 829\ 121\ 311\ (10)\text{kHz}$$

finding the Doppler-broadened absorption profile was not very difficult once the right temperature of the cell was found.

Also the Lamb-dip was well pronounced when the beam overlap was adjusted correctly due to an extreme power-broadening.

[4] unfortunately experimentally confirmed by us.

By measuring the frequency of the Lamb-dip relative to the cavity resonance repeatedly, we discovered a strong drift, which we could correlate with the change of the remaining gas pressure inside the cavity housing caused by a leak. This correlation can be explained by the pressure dependence of the refractive index of air, which determines the free spectral range and thus the absolute position of the resonance.

As attempts to reduce the leakage rate to a magnitude which would not induce any significant drift failed, we used an old ion getter pump to keep the pressure at an equilibrium (monitored over two weeks) of ca. 10^{-3}mBar, which is within a region where slight pressure changes have no big influence on the resonance frequency.

We could determine the resulting relevant resonance, close to it's absolute vacuum value, to be at a frequency ca. 505MHz higher than the atomic resonance. This led us to chose a 350Mhz AOM in double pass configuration running at 252.5MHz.

5.3.1 Refractive index shift

The refractive index of the cavity medium is very important for the absolute positions of the resonances. Even small variations cause a significant shift.

The refractive index n is a scaling factor for the wavelength. Hence frequency and free spectral range scale inversely with n

$$\nu^{(n)} = \frac{\nu_0^{(\mathrm{vac})}}{n} \qquad \nu_{\mathrm{FSR}}^{(n)} = \frac{\nu_{\mathrm{FSR}}^{(\mathrm{vac})}}{n}$$

If ν_0 is a specific resonance, the shift induced by a refractive index $n = 1 + m$ is given as

$$\Delta\nu^{(n)} = \nu_0^{(\mathrm{vac})} - \nu^{(n)} = \nu_0^{(\mathrm{vac})} \cdot \frac{m}{n} \approx m \cdot \nu_0^{(\mathrm{vac})}$$

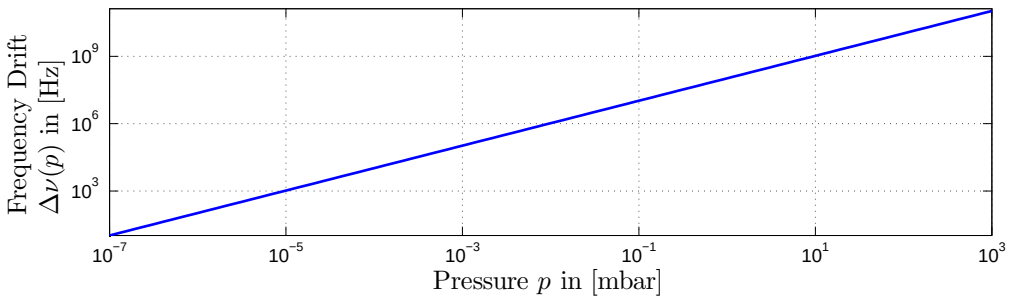

Figure 5.4: The frequency drift $\Delta\nu^{(n)}$ of a resonance at 689nm caused by air at 35.9°C, 30% humidity within a pressure range of 10^{-3} to 10^{-7}mBar.

Fig. 5.4 shows the drift of a resonance at 689nm, when the pressure dependence of the refractive index is calculated according to the Edlén formula [12].

6 ^{88}Strontium $(5s^2)^1S_0 \rightarrow (5s5p)^3P_1$ Spectra

6.1 Spectra

The spectra in fig. 6.1 show the Lamb-dip of the $(5s^2)^1S_0 \rightarrow (5s5p)^3P_1$ transition. They have been created by acquiring the signal of PD:Sat and PD:Back at a sample rate of 1.5MHz while ramping the frequency of the frequency generator that drives the AOM with an external DC voltage.

The frequency was incremented in 1000 steps of 1kHz each. For each step 2000 samples were averaged. Despite this averaging, the signal stayed noisy since the principal frequency instability of the laser manifests itself at low frequencies. Therefore the shown spectra were created by averaging about 20 sequential scans, which have been shifted slightly so that the center of a Lorentz fit coincides.

To account for the intensity fluctuations caused by the frequency dependent diffraction efficiency of AOM the spectra have been divided a background signal representing fix fraction of the light power before entering the cell, recorded with the photodiode PD:Back. Dividing the signal does not complete compensate for the intensity fluctuations, because the signal of the saturation spectroscopy is non linear. The background, as shown in the last plot, was acquired analogously.

The blue solid lines show a Lorentzian fit to the spectrum with the resulting FWHM Γ denoted within them. The sequence of plots from left to right, top to bottom, shows the results for decreasing probe beam powers. For all spectra the Lorentzian fit shows good agreement, but noise increases dramatically for low powers. The decreasing width can be related to the decreasing power broadening.

Symmetrically to the right and left, some structures appear, which might be accounted for by the Zeeman effect, which causes the $m_J = \pm 1$ states to split symmetrically.

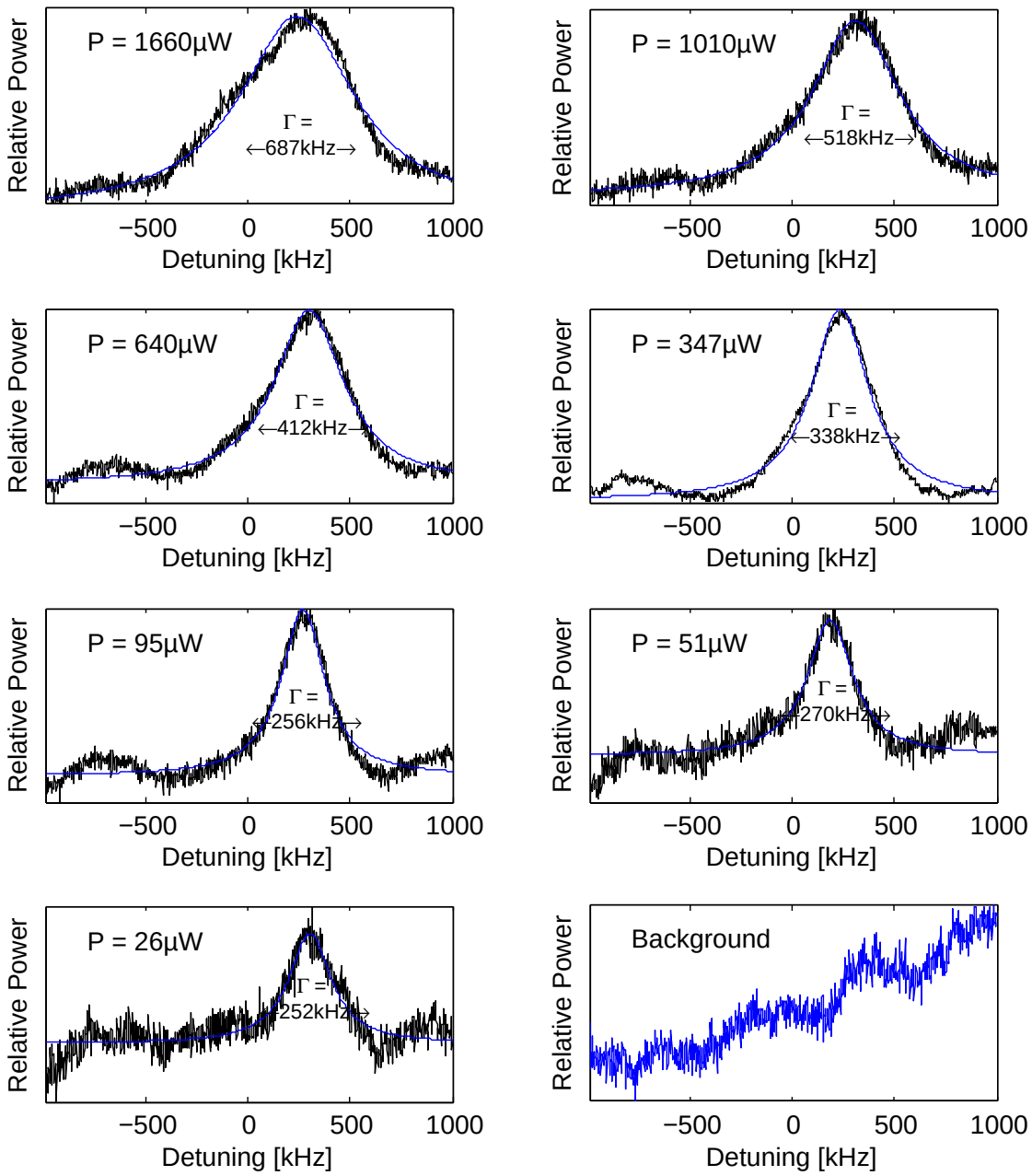

Figure 6.1: The Lamb-dip of the $(5s^2)^1S_0 \rightarrow (5s5p)^3P_1$ transition of ^{88}Sr, obtained via saturation spectroscopy, for various powers P of the saturation beam. The scan of ±1Mhz was obtained by a double pass AOM configuration. The scales of the frames vary for better visibility. The last frame shows the signal recorded on PD:Background in fig. 3.7 which reflects the performance of the AOM.

6.2 Broadening and shifts

6.2.1 Power broadening

Power broadening describes the fact that the width of spectral lines increases with the light intensity used. This can be explained by the non-linearity of the absorption coefficient with intensity. Instead it saturates, due to the fixed number of atoms contributing, their finite decay rate and stimulated emission. Hence with increasing intensity the spectral absorption line grows least at frequencies where most photons are absorbed and vice versa. This deformation preserves the Lorentzian line shape but increases the linewidth Γ [15]

$$\Delta\omega_{\mathrm{FWHM}} = \Gamma\sqrt{1 + \frac{I}{I_{\mathrm{Sat}}}}$$

where the saturation intensity is given by

$$I_{\mathrm{Sat}} = \frac{1}{12}\frac{\hbar\Gamma}{\pi c^2}\omega^3$$

As the sequence of plots in fig. 6.1 shows, we can observe a clear dependance of the linewidth on the used intensity, and the smallest width of 256kHz is still approximately 34 times the natural linewidth. This means the line is broadened by at least one broadening mechanism. Because the saturation intensity of the narrow line is so weak ($I_{\mathrm{Sat}} = 3.03\frac{\mu\mathrm{W}}{\mathrm{cm}^2}$), power broadening is the first candidate to be investigated.

Plotting the linewidth against the used power shows a rather linear behavior, c.f. fig. 6.2.

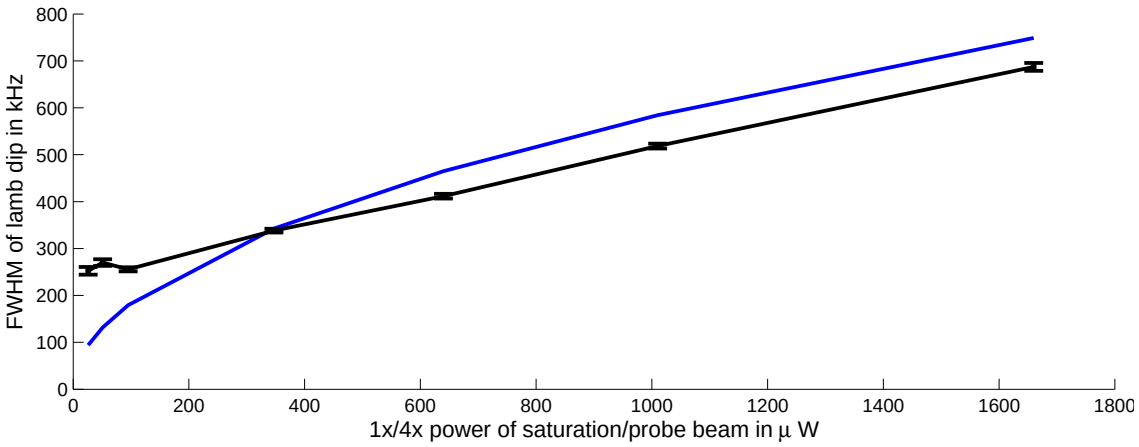

Figure 6.2: FWHM vs power of the probe beam, black line with error bars. The blue line shows the theoretically expected intensity broadening.

To compare the results with the theoretical value, a perfectly homogeneous beam profile with a diameter corresponding to the beam $\frac{1}{e^2}$-diameter of the Gaussian beam

is assumed. The measured 2.7 mm result in an active beam area of 5.6mm^2 for which the saturation power computes to 0.17µW. This means that even the lowest used powers saturate the atoms strongly. The solid blue line in fig. 6.2 shows the theoretically expected FWHMs.

For the lowest three probe powers the expected width is smaller which indicates that another broadening mechanism becomes relevant. In general the dependency of the FWHM on the beam power seems to resemble a rather linear than expected square root dependency.

To estimate the statistical error of the FWHM width caused by the noise of the photodiode signal the error bars of the Lorentzian fit were determined. This was achieved with a Monte-Carlo method as presented in [3], chap. 4.2.3. Consider the spectrum data points $v(k)$, shown in black in fig. 6.1, and the data points $l(k)$ describing the fitted Lorentzian, shown in blue in the same figure. The fit converged up to a certain standard deviation of $(v-l)$. The error was calculated by generating a set of new random spectra $v_i^{rand}(k)$ that have the same standard deviation from l

$$v_i^{rand}(k) = l(k) + \mathrm{DEV}(v-l) \cdot \mathrm{RAND}_i$$

where DEV represents the standard deviation and RAND a set of random numbers with unit standard deviation and zero mean. For each of those data sets the same Lorentzian fit as for the original data was conducted. The resulting distribution of FWHM widths now has the a mean value corresponding to the original width, but also allows to determine the error by calculating its standard deviation.

6.2.2 Collisional broadening and shifting

When considering a gas of a mixture of atoms rather than an individual atom, the mutual interaction has to be taken into account. When an atom that is interacting with a light field comes close to another atom the electromagnetic interaction of the shell electrons causes a shift of its energy levels, which alters its oscillation phase and frequency. For a statistical ensemble of atoms, there one may observe a shift and broadening of the resonances depending on the temperature and pressure of the gas.

The influence of the interaction can sufficiently be described a cross section each, for shifting and broadening, that has been determined experimentally for our case of strontium in argon buffer gas ([16] for Sr-Ar and [9] for Sr-Sr) . Bidel [4] presents a calculus for the blue 461nm line based on a paper by Chan and Gelbwachs [6], that also applies for the investigated red 689nm intercombination line.

Collisional broadening is a so called linear broadening mechanism, that means that the Lorentzian shape of the natural line is preserved while the natural FWHM Γ_{nat} increases by an addend

$$\frac{\Gamma_{\mathrm{tot}}}{2\pi} = \frac{\Gamma_{\mathrm{nat}}}{2\pi} + \frac{\Gamma_{\mathrm{coll}}}{2\pi}$$

The increased width is determined from the average relative speed $\overline{v}$ between the atoms, the shifting cross section $\sigma_{\text{Sr-Ar}}^{(\text{broad})}$ and the gas density n_{Ar}

$$\Gamma_{\text{coll}} = \frac{1}{\pi}\,\sigma_{\text{Sr-Ar}}^{(\text{broad})}\,\overline{v}\,n_{\text{Ar}}$$

with

$$\overline{v} = \sqrt{\frac{8k_{\text{B}}T}{\pi\mu}} \qquad \frac{1}{\mu} = \frac{1}{m_{\text{Sr}}} + \frac{1}{m_{\text{Ar}}}$$

$$\sigma_{\text{Sr-Ar}}^{(\text{broad})} = 1.57(0.02)\cdot 10^{-14}\text{cm}^2$$

$$n_{\text{Ar}} = \frac{P_{\text{Ar}}}{k_{\text{B}}T}$$

To determine the impact of pressure broadening on the spectra in fig. 6.2, it is necessary to know the exact pressure within the cell. Unfortunately the setup did not yet include a pressure gauge at the time the measurements were made and it might be possible that a leak or insufficient backing caused collisional broadening that would significantly increase the linewidth.

Only an estimation can be made about the pressure that must have prevailed for causing a broadening up to $\Delta\nu = 250\text{kHz}$. Reformulating the above equations it follows that

$$P > k_{\text{B}}T \cdot \frac{2\pi^2\Delta\nu}{\sigma_{\text{Sr-Ar}}^{(\text{broad})}\overline{v}}$$

For a temperature of 500°C the pressure necessary for causing the observed broadening would be

$$P_{\text{broad}} = 4.3\cdot 10^{-1}\text{mBar}$$

This means that for causing such a broadening a significant amount of air must have entered and the cross section of air should be taken into account.

The expected broadening, of the approximately $3\cdot 10^{-3}$mBar that was measured at the time of filling the oven, scales linearly to about 1.7kHz.

The broadening caused by collisions between the strontium atoms themselves can be calculated in the same manner, using the partial pressure as discussed in sec. 2.1.3 and

$$\sigma_{\text{Sr-Sr}}^{(\text{broad})} = 6.55(0.6)\cdot 10^{-14}\text{cm}^2$$

which yields a broadening of

$$\Delta\nu_{\text{Sr-Sr}} = 9.5\text{kHz}$$

6.2.3 Transient broadening

Transient broadening describes the fact that the atoms contributing to the Lamb dip have despite the zero velocity in the direction of the optical axis, still have a thermal velocity distribution perpendicular to it and thus may leave the light beam

during the interaction creating an upper limit in interaction time, which translates in the Fourier transformed domain of emission frequencies into a minimal linewidth.

This fact can be expressed as an energy-time-uncertainty analogously to the description of the relation of the natural linewidth with the finite lifetime due to spontaneous emission

$$\Delta E \Delta t \gtrsim h$$

The linewidth becomes

$$\frac{\Gamma}{2\pi} = \frac{1}{\tau_{\mathrm{nat}}} + \frac{1}{\tau_{\mathrm{IA}}}$$

where τ_{IA} is the characteristic interaction time.

In our case with a $\frac{1}{e^2}$ beam diameter that has been determined to 2.7mm and a median gas velocity of $391\frac{\mathrm{m}}{\mathrm{s}}$, a characteristic interaction time of 6.9µs leads to a line broadening of

$$\frac{\Gamma}{2\pi} = 145\mathrm{kHz}$$

This is already very close to the observed limit. Attempts have been made to use a bigger beam diameter, but they did not show any improvements, which indicates that another broadening mechanism is prevailing.

6.2.4 Zeeman effect

The Zeeman Effect describes the splitting of spectral lines of atoms in weak magnetic fields. It is caused by the atomic magnetic moment interacting with the external field and thus separating the previously degenerate states of different orientations of the magnetic moment.

The energy of the magnetic moment in the magnetic field B can be calculated as

$$\Delta E_{\mathrm{Zeeman}} = m_J \, \mu_{\mathrm{B}} g_{\mathrm{J}} \, |B|$$

where m_J is the quantum number of the total angular momentum operator J_z, μ_{B} is the Bohr magneton and g_j the Landé factor given by

$$g_J = 1 + \frac{J(J+1) + S(S+1) - L(L+1)}{2J(J+1)}$$

with J and S being the quantum numbers associated with the total angular and spin momentum operators J^2 and S^2 respectively.

For both of the main transitions relevant in the cooling process, a Zeeman splitting into triplets occurs. The g-factors for the involved states are:

$$^1S_0 : g_j = 1$$
$$^1P_1 : g_j = 1$$
$$^3P_1 : g_j = 1.5$$

Within an earth magnetic field of 23µT in Sao Carlos [2], the corresponding shifts are

$$^1S_0 \rightarrow {}^1P_1\text{: } \Delta\nu_{\text{Zeeman}} = 322\text{kHz}$$
$$^1S_0 \rightarrow {}^3P_1\text{: } \Delta\nu_{\text{Zeeman}} = 483\text{kHz}$$

These values are only rough estimates, since the application of the Landé factor supposes pure LS coupling and strontium as a medium weighted atomic species, is governed by a mixture between JJ and LS coupling, while LS is still dominating [23]. The $^3P_1$ denominated state therefore contains a small admixture of the $^1P_1$ component, which in the first place renders the intercombination with the ground state possible. The value of the frequency offset should thus be expected smaller.

This predicted splitting of the different Zeeman levels due to gravitation of 483kHz could be identified with the flat peaks at a distance of about 1MHz from the central resonance. Introducing an additional magnetic field did shift these peaks further away from the center, indicating that their origin indeed is the Zeeman shift.

The mismatch with the estimated value might be caused by additional stray magnetic fields in the order of magnitude of the earth magnetic field. Further measurements of the background magnetic field would be necessary to gain certainty about the origin of the shift.

7 Résumé and outlook

This work describes the realization of a Pound Drever Hall stabilization of a diode laser onto the atomic resonance of the ${}^1S_0 \rightarrow {}^3P_1$ transition of strontium. This stabilization is necessary for creating an efficient magneto optical trap (MOT) that operates on this, only 7.6 kHz wide, transition.

Therefore the aspired linewidth of the laser system was 1kHz. An estimated width of 600Hz has been achieved, even though disturbed by fluctuations in the Hz regime. For long term stabilization a spectroscopy was constructed that resolves the line with a minimally widened width of 252kHz.

The Pound Drever Hall technique allows us to derive a frequency error signal, which can be used for an electronic feedback loop to correct the diode laser current, from a light beam that is reflected from an optical oscillator. The reflection of light from an optical resonator is strongly dependent on its frequency. Resonant frequencies that interfere constructively within the resonator are transmitted and non resonant frequencies are reflected. Deriving the error signal from the intensity of the reflected light bears two disadvantages. Firstly, with this error one cannot distinguish between frequency and intensity fluctuations and secondly the error signal is delayed, because the interference needs time to build up inside the resonator.

To circumvent these problems, the phase information of the reflected beam can be used. Ideally the phase does not show any intensity dependence and is measured between a promptly reflected beam and the field that has already been built up inside the resonator.

The stabilization has been realized with a 10cm long symmetric cavity[1] of finesse 600 formed by a pair of mirrors with a radius of curvature of 50cm, that were optically contacted to an ULE[2] spacer. The cavity is placed into a special housing[3] which provides vacuum and a constant temperature in order to keep the resonance stable.

The stability of the locked laser has been estimated by measuring the error signal and the discriminator, which is the conversion factor to translate an error into a frequency deviation. The data of frequency deviations has then been analyzed by calculating the power spectral density of frequency fluctuations and the Allan variance of the normalized frequency. This allowed to deduce the line widths of the laser for five different measurement series. In one of which a stabilitiy of 600Hz was reached.

[1] produced by Advanced Thin Films
[2] Ultra Low Expansion material from Corning
[3] Manufactured by Stable Laser Systems

Using the stabilized laser a saturation spectroscopy has been conducted. The frequency of the laser was scanned with an AOM, in double pass configuration to avoid disalignment, within 2MHz around the Lamb dip of the investigated transition. The spectra show a broadened dip of a minimum FWHM width of 252kHz and the splitting of the $^3P_1$ level into three Zeeman sublevels caused by some stray magnetic fields. The discussion of the broadening mechanism suggests that it is the transient broadening, which dominantly causes the increased linewidth.

The next step would be to use the spectroscopy as an absolute reference to analyze drifts of the laser frequency, which has only been stabilized relative to the cavity. If a strong drift can be observed, electronics for a long term stabilization need to be developed. An additional AOM between the cavity and the experiment could then compensate for this drift.

Finally, once the main experiment progressed to the stage where cold atoms are trapped in a primary stage MOT on the $^1S_0 \rightarrow^1 P_1$ transition, the stabilized laser can be used for implementing a secondary stage MOT.

Bibliography

[1] D.W. Allan and J.A. Barnes, *A modified Allan variance with increased oscillator characterization ability*, Thirty Fifth Annual Frequency Control Symposium. 1981, IEEE, 1981, pp. 470–475.

[2] Wolfram Alpha, *Wolfram Alpha LLC*, 2011.

[3] Helmar Bender, *Quantenoptik an Oberflächen - Untersuchung von Atom/Oberflächen-Wechselwirkungen durch Reflektion von Bose-Einstein Kondensaten an Materiewellen-Spiegeln*, Ph.D. thesis, Universität Tübingen, Wilhelmstr. 32, 72074 Tübingen, 2011.

[4] Y. Bidel, *Piégeage et refroidissement laser du strontium, Etude de l'effet des interférences en diffusion multiple*, Ph.D. thesis, PhD thesis, Université de Nice-Sophia Antipolis, 2002, S. 92 ff, 2002.

[5] E.D. Black, *An introduction to Pound–Drever–Hall laser frequency stabilization*, American Journal of Physics **69** (2001), 79.

[6] YC Chan and JA Gelbwachs, *Broadening, shifting and asymmetry of the strontium resonance line induced by rare gas perturbers*, Journal of Physics B: Atomic, Molecular and Optical Physics **25** (1992), 3601.

[7] Philippe W. Courteille, *Frequenzstabilisierung eines Helium Neon Lasers und Langzeitstabilisierung eines externen Resonators*, Master's thesis, Universität Hamburg, 1989.

[8] I. Courtillot, A. Quessada, RP Kovacich, JJ Zondy, A. Landragin, A. Clairon, and P. Lemonde, *Efficient cooling and trapping of strontium atoms*, Optics letters **28** (2003), no. 6, 468–470.

[9] J.K. Crane, M.J. Shaw, and RW Presta, *Measurement of the cross sections for collisional broadening of the intercombination transitions in calcium and strontium*, Physical Review A **49** (1994), no. 3, 1666.

[10] W. Demtröder, *Atoms, molecules and photons: an introduction to atomic-, molecular-, and quantum-physics*, vol. 1439, Springer Verlag, 2006.

[11] RWP Drever, J.L. Hall, FV Kowalski, J. Hough, GM Ford, AJ Munley, and H. Ward, *Laser phase and frequency stabilization using an optical resonator*, Applied Physics B: Lasers and Optics **31** (1983), no. 2, 97–105.

[12] B. Edlén, *The refractive index of air*, Metrologia **2** (1966), 71.

[13] A. Einstein, *Sitzungsber. Preuss. Akad. Wiss. 1924, 261; ibid. 1925, 3; SN Bose*, Z. Phys **26** (1924), 178.

[14] G. Ferrari, P. Cancio, R. Drullinger, G. Giusfredi, N. Poli, M. Prevedelli, C. Toninelli, and GM Tino, *Precision frequency measurement of visible in-*

tercombination lines of strontium, Physical review letters **91** (2003), no. 24, 243002.

[15] C.J. Foot, *Atomic physics*, vol. 7, Oxford University Press, USA, 2005.

[16] J.C. Holtgrave and P.J. Wolf, *Pressure broadening and line shifting of atomic strontium (5s2) 1S0 -> (5s5p) 3P1 and (5s5p) 3P(0,1,2) -> (5s6s) 3S1 absorption transitions induced by noble-gas collisions*, Physical Review A **72** (2005), no. 1, 012711.

[17] R.E. Honig and D.A. Kramer, *Vapor pressure data for the solid and liquid elements*, RCA review **30** (1969), no. June, 285–305.

[18] Corning Incorporated, *ULE® Corning Code 7972 Ultra Low Expansion Glass*, Corning Incorporated, www.corning.com.

[19] K.H. Ko, Y.K. Lim, D.Y. Jeong, H. Park, T.S. Kim, G. Lim, and H. Ki Cha, *Measurement of the isotope selectivity of the strontium magneto-optical trap by a time-of-flight mass spectrometer*, JOSA B **23** (2006), no. 12, 2465–2469.

[20] H. Kogelnik and T. Li, *Laser beams and resonators*, Proceedings of the IEEE **54** (1966), no. 10, 1312–1329.

[21] Sebastian Kraft, Felix Vogt, Oliver Appel, Fritz Riehle, and Uwe Sterr, *Bose-Einstein Condensation of Alkaline Earth Atoms:* ^{40}Ca, Phys. Rev. Lett. **103** (2009), 130401.

[22] D.R. Lide, *CRC handbook of chemistry and physics: a ready-reference book of chemical and physical data*, CRC Pr I Llc, 2004.

[23] A.D. Ludlow, *The strontium optical lattice clock: Optical spectroscopy with sub-hertz accuracy*, Ph.D. thesis, 2008.

[24] AD Ludlow, X. Huang, M. Notcutt, T. Zanon-Willette, SM Foreman, MM Boyd, S. Blatt, and J. Ye, *Compact, thermal-noise-limited optical cavity for diode laser stabilization at 1× 10< sup>- 15</sup>*, Optics letters **32** (2007), no. 6, 641–643.

[25] T.H. Maiman, *Stimulated optical radiation in ruby*, (1960).

[26] The Mathworks Inc., *Matlab R2011b Documentation*.

[27] PG Mickelson, Y.N.M. De Escobar, M. Yan, BJ DeSalvo, and TC Killian, *Bose-Einstein condensation of^{88} Sr through sympathetic cooling with^{87} Sr*, Physical Review A **81** (2010), no. 5, 051601.

[28] W. Paul and H. Steinwedel, *Ein neues massenspektrometer ohne magnetfeld*, Zeitschrift Naturforschung Teil A **8** (1953), 448.

[29] EL Raab, M. Prentiss, A. Cable, S. Chu, and D.E. Pritchard, *Trapping of neutral sodium atoms with radiation pressure*, Physical Review Letters **59** (1987), no. 23, 2631–2634.

[30] W.J. Riley, Physics Laboratory (US). Time, and Frequency Division, *Handbook of frequency stability analysis*, US Dept. of Commerce, National Institute of Standards and Technology, 2008.

[31] R. Shiavi, *Introduction to applied statistical signal analysis: guide to biomedical and electrical engineering applications*, Academic Press, 2007.

[32] F. Sorrentino, G. Ferrari, N. Poli, R. Drullinger, and GM Tino, *Laser cooling and trapping of atomic strontium for ultracold atom physics, high-precision spectroscopy and quantum sensors*, Arxiv preprint physics/0609133 (2006).

[33] S.R. Stein, *12 Frequency and Time-Their Measurement and Characterization*, (1985).

[34] S. Stellmer, M.K. Tey, R. Grimm, and F. Schreck, *Bose-Einstein condensation of 86Sr*, Arxiv preprint arXiv:1009.1701 (2010).

[35] S. Stellmer, M.K. Tey, B. Huang, R. Grimm, and F. Schreck, *Bose-Einstein condensation of strontium*, Physical review letters **103** (2009), no. 20, 200401.

[36] D.B. Sullivan, National Institute of Standards, and Technology (US), *Characterization of clocks and oscillators*, US Dept. of Commerce, National Institute of Standards and Technology, 1990.

[37] E. Arimondo J. L. Hall T. P. Dinneen, K. R. Vogel and A. Gallagher, IEEE Trans. Instrum. Meas. **42** (1993), 115.

[38] U. Tietze, C. Schenk, and E. Gamm, *Halbleiter-schaltungstechnik*, vol. 11, Springer, 1971.

Acknowledgments

I would like to thank everybody that helped me during the last 15 months with my thesis. First of all I would like to thank my adviser Philippe Courteille for always taking the time to answer my questions and for all his effort in bringing together our new group. I also thank the other group members Andrés, Helmar, Romain, and Maria Luiza for advice and especially all the good time we passed together inside and outside the lab. I won't forget the the endurance and motivating words from Alessandro and Helmar during the long nights of measurements.

Special thanks go to the whole grupo de ôptica, and oficina mecanica for all the patience they brought up helping us out by lending us a lot of equipment and dealing with both cultural and linguistic misunderstandings. Thank you Isabel, Chritiane and Bené for all your support dealing with hundreds of burocratical issues.

I am thankful for the hospitality with which I was received in Brazil by so many cordial people, like Marilde and Philippe, my neighbors, Ozzy and Negao, everyone at the Tuesday dinners and many more.

Thank you Astrid, for your patience and energy that made it possible to overcome our separation by an ocean.

I thank the Palazzo WG in Tübingen for creating a perfect home for me during the last days of completion of my thesis, especially David and Chris for proof-reading.

I am grateful for the financial support I received for the first six months from the DAAD and during the last three months from the CNPq.

Finally I want to thank everybody I forgot in the above mentioned.

Erklärung

Hiermit erkläre ich, dass ich die vorliegende Arbeit selbstständig und unter ausschließlicher Verwendung der angegebenen Quellen angefertigt habe.

Tübingen, den 9. Januar 2012

Dominik Vogel